Comput Geosci (2016) 20:835–856
DOI 10.1007/s10596-015-9527-2

ORIGINAL PAPER

Multiphase flow modeling with density functional method

Oleg Dinariev[1] · **Nikolay Evseev**[1]

Received: 27 February 2014 / Accepted: 4 September 2015 / Published online: 29 September 2015

Abstract This paper is a review of applications of density functional theory (DFT) in compositional hydrodynamics. The basic idea is representation of the entropy or the Helmholtz energy of the mixture as the functional depending on the molar densities of chemical components (density functional). The hydrodynamics is governed by local conservation laws of chemical components, momentum, and energy, while constitutive relations and boundary conditions are introduced in accordance with the explicit form of the density functional. The general ideas and the history of the DFT in compositional hydrodynamics are discussed. Then the DFT for multiphase multicomponent mixtures is presented including the exposition of the first principles, governing equations and constitutive relations, and explicit expressions of density functional depending on physical situation. The DFT-based numerical simulator is described, and several multiphase simulation results are presented to illustrate the scope and effectiveness of DFT: sessile drop with and without surfactant, droplet breakup in shear flow, and three-phase hydrodynamics with mobile solid phase. Also, two practical scenarios with multiphase simulations in micro-CT porous rock models are presented: two-phase immiscible water-oil flow and three-phase water-gas-condensate flow with phase transitions. All numerical results are obtained by essentially the same code; both the number of chemical components and the Helmholtz energy have been set up in accordance with physical situation.

✉ Nikolay Evseev
nevseev@slb.com

[1] Schlumberger Moscow Research, 13, Pudovkina Street, Moscow 119284, Russia

Keywords Density functional theory · Entropy · Helmholtz energy · Multiphase hydrodynamics · Numerical modeling

1 Introduction

The modeling approach to the pore-scale processes in hydrocarbon reservoirs should satisfy several requirements. First, it must take account of the complex chemical composition of the reservoir fluids and describe changes in composition caused by phase transitions and chemical reactions. Second, the exact number of phases in the reservoir mixture is not predetermined and constitutes one of the unknown quantities. Moreover, the number and the nature of phases in the mixture can change with time being dependent on the processes in the reservoir. For example, the gas-condensate deposits are usually characterized by two-phase initial state of the mixture containing aqueous solution and hydrocarbon gas. When the gas is recovered, drop in reservoir pressure can cause retrograde condensation with appearance of third liquid hydrocarbon phase. Then, under certain development schemes, dry gas can be injected into the reservoir, and this can result in local evaporation of water and condensate with gas as the only remaining phase.

Third, the spatial distribution of phases is not predetermined and can evolve in time. Thus, the modeling approach should be sufficiently flexible and efficient to handle the complex dynamics of interfacial boundaries. Fourth, the description of phase transitions should cover near-critical region and, therefore, cannot be based on phase indicator or phase saturation concepts. Indeed, variables of this kind cannot be defined continuously in the vicinity of critical points.

These requirements are satisfied in the framework of the density functional theory (DFT) hydrodynamics, or, more shortly, the density functional hydrodynamics (DFH), which relies on the molar density fields of chemical components constituting the mixture. The thermodynamic model is based on Helmholtz energy (or entropy), which is a function of molar densities. The new system of dynamic equations obtained within the DFT framework represents M scalar equations for conservation of chemical components, three scalar equations for conservation of momentum, and a scalar equation for total energy conservation with constitutive relations consistent with density functional (Section 2). The basic density functional contains molar density gradient terms, which produce higher order spatial partial derivatives in hydrodynamic equations (Section 3). Additional equations are introduced for complex systems containing mobile solid phases with or without structural defects (Section 4).

Section 5 discusses the DFH numerical simulator, while Section 6 presents several multiphase numerical solutions, which demonstrate the capabilities of DFH. Finally, the capabilities of the method are demonstrated by simulation of a two pore-scale multiphase flow scenarios related to oil and gas production (Section 7).

The origins of DFT can be traced to the model by Thomas [57] and Fermi [23] developed in 1927. This quantum mechanical model was used in describing inhomogeneous ground state electron configurations; however, the modern DFT originates in the 1964 works by Kohn and his coauthors [27, 32]. In the following years, the DFT found its place in many disciplines of physics; see reviews in [20, 22, 31, 45].

The applications of DFT in compositional hydrodynamics can be traced to [11] in isothermal formulation. In 1998, the theory was extended for non-isothermal cases [12]. Since then, a large experience was accumulated in DFT numerical applications for different multiphase problems with or without phase transitions. A significant part of it is covered by our book [9]. In the present review, we have tried to reach a balance between fundamentals and applications.

There are many similar approaches to the description of interfaces, which are based on introduction of gradient terms for phase transition zones [1, 53]. Though quite effective in their respective areas of applications, they are not adequate for the whole set of possible processes in hydrocarbon reservoirs. For instance, concentration gradients are not indicative for azeotropic mixtures, while mass density gradients are not indicative for two-phase mixtures with low mass density contrast. More detailed comparative discussion of different methods in multiphase hydrodynamics can be found in [9, 10].

In the following text, the number of different chemical components in the mixture is denoted by M. The indices i, j, and k correspond to the component numbers and take values $1, ..., M$. The indices a and b correspond to the Cartesian coordinates x^a or curvilinear coordinates y^a and take values 1, 2, and 3. We use shortened notations for partial derivatives in respect to Cartesian coordinates $\partial_a = \partial/\partial x^a$, time $\partial_t = \partial/\partial t$, and molar density of the ith chemical component $\partial f_{,i} = \partial f/\partial n_i$. By default, the summation is carried out over the repeated indices. In Cartesian coordinates, the tensors with up or down indices are identical.

2 Physical foundations

We describe the multicomponent mixture using the concepts of continuum mechanics. The mixture is represented as a medium, which is continuously distributed in space. The molecules are not resolved as objects with individual parameters. Instead, we deal with certain integral parameters, which characterize the mixture as a system of molecules. The continuum mechanics is applicable for fluids in pores when molecular free path is significantly smaller than the typical size of the pore. This condition is satisfied for many natural hydrocarbon reservoirs (but not for all). In order to incorporate capillary phenomena in our description, we expand classical continuum medium concepts by allowing local values of fluid parameters outside the thermodynamic stability range in the bulk.

The primary variables are assumed to be molar density of chemical components n_i, mass velocity v_a of the medium, and internal energy density u. For the homogeneous mixtures, which stay at rest or maintain uniform translational motion, these parameters are constant in time and space. In general case, these parameters can be variable fields. Let us recall definition for n_i, v_a, and u.

We consider spatial region D with volume V_D. Suppose that at a given instant of time t in this region the total number of molecules (in moles) of a component with the number i is $N_{iD} = N_{iD}(t)$. The molar density of the component with the number i at point with coordinates x^a is defined as the limit of the ratio of N_{iD} to V_D, when the volume V_D tends to zero, and D becomes infinitesimal vicinity of the point x^a

$$n_i = n_i(t, x^a) = \lim_{V_D \to 0} \left(\frac{N_{iD}}{V_D} \right). \tag{1}$$

Like in any continuous medium concept, here the transition to zero volume V_D is understood conventionally: it is assumed that the characteristic size of the domain D goes down but remains significantly larger than the molecular dimensions.

The molecules in the considered region D possess kinetic and potential energy. Summarizing all terms of the energy, we obtain some quantity $E_D = E_D(t)$. The energy density of a mixture is defined as the limit of the ratio of E_D to V_D

as the volume V_D tends to zero (with the same conventions as those assumed in Eq. 1)

$$\varepsilon = \varepsilon(t, x^a) = \lim_{V_D \to 0} \left(\frac{E_D}{V_D} \right). \tag{2}$$

In order to define molecular fluxes within the medium, let us consider a surface element with unit normal vector l_a and area ΔA. A number of molecules ΔN_i (in moles) of the component i passing through the surface element in the direction of l_a per unit time are approximately proportional to the value of ΔA. Thus, it is possible to introduce the flux vector I_{ia} of this component as the following:

$$l_a I_{ia}(t, x^b) = \lim_{\Delta A \to 0} \left(\frac{\Delta N_i}{\Delta A} \right). \tag{3}$$

Using molar masses of chemical components m_i, one can calculate the total mass flux $I_a = m_i I_{ia}$ and the mass density of the mixture $\rho = m_i n_i$. After that, the mass velocity is defined by the following equation

$$v_a = v_a(t, x^b) = \frac{I_a(t, x^b)}{\rho(t, x^b)} \tag{4}$$

The difference between the total flux of molecules and the convective transport is the diffusion flux

$$Q_{ia} = Q_{ia}(t, x^b) = I_{ia} - n_i v_a. \tag{5}$$

Also, we can introduce the internal energy of a mixture as the difference between the total energy and the kinetic energy or, equivalently, the energy in the frame of reference, where the medium is locally at rest

$$u = u(t, x^a) = \varepsilon - \frac{1}{2} \rho v_a v_a. \tag{6}$$

Since the quantities n_i, v_a, and u are assumed to be the primary variables, all other variables can be calculated from n_i, v_a, and u according to certain rules. In particular, one can calculate the entropy S_D of the mixture.

It is important to make several remarks concerning the concept of the entropy in continuum mechanics. In one-phase hydrodynamics or fluid dynamics, the mixture is usually represented as an aggregate of locally equilibrium subsystems, which are continuously distributed in space and interact with each other by exchanging components, momentum, and energy [52]. In this case, the entropy is calculated by summation of the subsystem entropies. In multiphase mixtures, such approach is not valid, and the entropy must be considered as a functional of primary fields. The exact expression for the entropy functional can be derived in classical or quantum statistical mechanics [12, 14, 15, 59]. From a mathematical point of view the entropy is defined up to certain coefficient (Boltzmann constant) as information entropy [25, 42], while the information entropy is calculated for locally equilibrium Gibbs state associated with given distribution of primary fields $n_i(t, x^a)$, $v_a(t, x^b)$, and $u(t, x^a)$. This definition is consistent with second law of thermodynamics, which requires non-negative entropy production for non-equilibrium processes [13, 14] Also one can rigorously derive the independence of the entropy on the velocity field [59], as a remarkable corollary of the Galilean invariance

$$S_D = S_D[u, n_i]. \tag{7}$$

Notwithstanding the described well-known procedure for the calculation of the entropy it is but rarely used for practical problems, because it depends on insufficiently understood collective molecular interaction phenomena. Thus the effective way to deal with the entropy functional is to introduce certain explicit model expressions, which can be checked against existing experimental evidence and theoretical considerations. It is convenient to list theoretical requirements, which follow from the definition of entropy functional in classical or quantum statistical mechanics.

Entropy property 1 The entropy functional (7) is supposed to be continuous and differentiable at a suitable convex set in linear functional space of the fields of internal energy and of molar densities of components.

In accordance with property 1, one can calculate the variation of the entropy functional (7)

$$\delta S_D = \int_D (\Theta_0 \delta u + \Theta_i \delta n_i) dV + \Gamma_u[\delta u] + \Gamma_n[\delta n_i], \tag{8}$$

where there are following variational derivatives

$$\Theta_0 = \frac{\delta S_D}{\delta u}, \quad \Theta_i = \frac{\delta S_D}{\delta n_i}, \tag{9}$$

and the terms Γ_u and Γ_n denote linear boundary operators of the variations δu and δn_i, respectively.

Entropy property 2 In the particular case, when the boundary of the domain ∂D coincides with a solid surface that is homogeneous in its properties and the values of u and n_i are constants (i.e., the state of a mixture is homogeneous), then the entropy functional is reduced to the simple expression

$$S_D = s V_D + s_* A_{\partial D} \tag{10}$$

where $s = s(u, n_i)$ is the entropy density in the conventional equilibrium thermodynamics, $s_* = s_*(u, n_i)$ is the surface entropy density associated with the boundary surface between the mixture and the solid, and $A_{\partial D}$ is the area of this surface.

Considering well-known thermodynamic equation for absolute temperature $T^{-1} = \left(\frac{\partial s}{\partial u} \right)_{n_i}$ [1, 46] and Eq. 10 one has to identify the quantity Θ_0^{-1} with absolute temperature T with for homogeneous states of the mixture. Also for homogeneous states one can calculate $\Theta_i = -T^{-1} \kappa_i$,

where κ_i is the chemical potential of the component with number i. For inhomogeneous states of the mixture the quantity $T_S = \Theta_0^{-1}$ can be regarded as an extension of the definition of temperature. This is why it is suitable to introduce the following

Entropy property 3 The value of T_S is positive.

The entropy functional must be consistent with the zeroth law of thermodynamics [2], which states that in thermodynamic equilibrium, the temperature is constant everywhere within the system. Besides, the growth of the entropy as a result of internal dissipative processes is always associated with equalization of temperature. The following condition provides the required connection between the entropy growth and the temperature equalization.

Entropy property 4 The functional $(-S_D)$ is strictly convex over the variable u, when the distribution of n_i is fixed. In other words, for distributions of $u_1 = u_1(t, x^a)$, $u_2 = u_2(t, x^a)$, $n_i = n_i(t, x^a)$, and real number $\lambda \in [0, 1]$, the following inequality takes place

$$S_D[\lambda u_1 + (1-\lambda)u_2, n_i] \geq \lambda S_D[u_1, n_i] + (1-\lambda) S_D[u_2, n_i], \tag{11}$$

while the equality sign can be in the following cases only: (a) $u_1 = u_2$, (b) $\lambda = 0$, and (c) $\lambda = 1$.

The value of this property can be seen from the following statement.

Let us consider two distributions of the internal energy u_1 and u_2 with *the same total internal energy value*. If the field u_1 corresponds to some constant temperature, then

$$S_D[u_1, n_i] \geq S_D[u_2, n_i], \tag{12}$$

while the equality sign is achieved only when $u_1 = u_2$.

In order to prove this statement, it is convenient to define the auxiliary function of scalar argument $\lambda \in [0, 1]$

$$\psi(\lambda) = S_D[u_1 + \lambda(u_2 - u_1), n_i] - S_D[u_1, n_i] \tag{13}$$

By reason of the assumed conjectures and property 4, the function (13) satisfies the relations $\psi(0) = 0$, $\frac{d\psi}{d\lambda}(0) = 0$, $\frac{d^2\psi}{d\lambda^2}(\lambda) \leq 0$, while $\frac{d^2\psi}{d\lambda^2}(\lambda) = 0$, if and only if $u_1 = u_2$. Therefore, $\psi(1) \leq 0$, which is equivalent to Eq. 12. At that $\psi(1) = 0$, only if $u_1 = u_2$. The proof is finished.

Up to now, all discussion was conducted in the frame of Cartesian coordinate systems. Yet in some problems with complex geometry, it is convenient to use curvilinear coordinate systems. Thus, it is relevant to consider the extension of the theory for arbitrary coordinate systems. Let us assume by definition that in curvilinear coordinate system y^a the internal energy density and densities of mixture components are related to the corresponding values in the Cartesian system x^a by the following equations

$$u(y^c) = u(x^c)\left|\det(\partial x^a/\partial y^b)\right|, n_i(y^c) = n_i(x^c)\left|\det(\partial x^a/\partial y^b)\right|. \tag{14}$$

Entropy property 5 The functional (7) can be rewritten in a curvilinear coordinate system y^a as the functional depending on internal energy density $u(t, y^a)$, molar densities of chemical components of the mixture $n_i(t, y^a)$, and the metric tensor of the curvilinear coordinate system $g_{ab}(y^c) = \frac{\partial x^d}{\partial y^a} \times \frac{\partial x^d}{\partial y^b}$:

$$S_D = S_D[u, n_i, g_{ab}], \tag{15}$$

and the functional (15) is invariant with respect to any transformations of coordinates.

Varying the functional (15), one can write down the equation, which generalizes Eq. 8:

$$\delta S_D = \int_D (\Theta_0 \delta u + \Theta_i \delta n_i - 2^{-1}\Sigma^{ab}\delta g_{ab})\,|g|^{1/2}\,dy^1 dy^2 dy^3 + \Gamma_u[\delta u] + \Gamma_n[\delta n_i] + \Gamma_g[\delta g_{ab}] \tag{16}$$

where $g = \det(g_{ab})$ and Γ_g is the boundary operator acting on the variation of the metrics, and the set of new parameters Σ^{ab} is related to the variational derivative of the entropy in respect to the metrics

$$\Sigma^{ab} = -2\frac{\delta S}{\delta g_{ab}}. \tag{17}$$

This second-order tensor plays an important role in hydrodynamic processes. It will be shown below that this tensor is directly related to the static stress tensor of the mixture

$$\sigma^{ab} = T_S \Sigma^{ab}. \tag{18}$$

One can easily calculate (18) for homogeneous states of the mixture using property 2 and the result is the following:

$$\sigma^{ab} = -p\delta^{ab}, \tag{18a}$$

where p is the hydrostatic pressure and δ^{ab} is the Kronecker symbol.

The invariance of the expression (15) in respect to the coordinate transformations (see property 5) makes it possible to use the Noether's theorem [24, 33] for deriving the differential identity, which establish relations between variational derivatives Θ_0, Θ_i, and Σ^{ab}. In a curvilinear coordinate system, this identity has the following form:

$$\nabla_b \Sigma^{ab} = g^{ab} g^{-1/2}(u\partial_b(g^{1/2}\Theta_0) + n_i \partial_b(g^{1/2}\Theta_i)), \tag{19}$$

where ∇_a is the covariant derivative operator [52]. In the Cartesian coordinate system, expression (19) is simplified

$$\partial_b \Sigma_{ab} = u\partial_a \Theta_0 + n_i \partial_a \Theta_i. \tag{20}$$

Before the study of dynamic problems, it is helpful to consider stationary equilibrium states of a mixture. Let us start with a mixture, in which no chemical reactions take place. The total internal energy and the amount of matter of each chemical component can be computed in the Cartesian coordinates by the following:

$$U_D = \int\limits_D u dV + \int\limits_{\partial D} u_* dA, \tag{21}$$

$$N_{iD} = \int\limits_D n_i dV, \tag{22}$$

where u_* is the surface density of the internal energy of the mixture. The stationary equilibrium states can be found as critical points of the functional (7) constrained by conditions (21) and (22) assuming the left side of both Eqs. 21 and 22 is constant. The corresponding states of the mixture satisfy the variational equation

$$\delta S_D - \lambda_0 \delta U_D - \lambda_i \delta N_{iD} = 0, \tag{23}$$

where λ_0, and λ_i are Lagrangian multipliers. In order to derive the explicit expressions from Eq. 23, one should use Eq. 8. Then Eq. 23 can be reduced to the form

$$\begin{aligned} &\int\limits_D ((\Theta_0 - \lambda_0)\delta u + (\Theta_i - \lambda_i)\delta n_i) dV \\ &+ (\Gamma_0[\delta u] - \lambda_0 \int\limits_{\partial D} \delta u_* dA) + \Gamma_i[\delta n_i] = 0\,' \end{aligned} \tag{24}$$

which produces the following equilibrium conditions

$$\Theta_0 = \lambda_0, \tag{25}$$

$$\Theta_i = \lambda_i. \tag{26}$$

Boundary terms in the left-hand part of Eq. 24 should be used for setting up the boundary conditions on the fields u and n_i. We will discuss these boundary conditions in detail below for particular model entropy functionals. Here, it is important to note that Eq. 25 means the constant temperature $T_S = \lambda_0^{-1}$ all over the mixture. This demonstrates the consistency with the zeroth law of thermodynamics [2], which states that in thermodynamic equilibrium, the temperature is constant everywhere within the system.

Now let us consider a mixture, which can undergo a set of chemical reactions defined by

$$\upsilon_{Ii} C_i \leftrightarrow \upsilon'_{Ii} C_i. \tag{27}$$

Here, C_i is the symbol of a component with the number i, while υ_{Ii} and υ'_{Ii} are non-negative stoichiometric coefficients. The index I here and below takes values 1, ..., K corresponding to the chemical reaction number.

Due to chemical reactions (27), the chemical components are not conserved and Eq. 22 does not hold. In order to determine conserved combinations of quantities (22), it is convenient to introduce a set of numbers $\eta_{Ii} = \upsilon_{Ii} - \upsilon'_{Ii} (I = 1, ..., K;\ i = 1, ..., M)$, which can be interpreted as a set of K vectors in M-dimensional space. Let us select the basis ζ_{Ji} of K_1 vectors in the orthogonal complementary subspace to the vectors η_{Ii}. Here and below the indexes J and J' take values of 1, ..., K_1. Note that the orthogonal complementary subspace to the η_{Ii} is non-empty, because, by reason of conservation of mass in chemical reactions, the following identity is valid (remember that m_i is the mass of the mole of the ith component of the mixture)

$$m_i \eta_{Ii} = 0. \tag{28}$$

By definition, chemical reactions (27) conserve the following set of K_1 quantities

$$Z_{JD} = \zeta_{Ji} N_{iD} = \zeta_{Ji} \int\limits_D n_i(x^a) dx^a. \tag{29}$$

Equilibrium states of the mixture in the presence of chemical reactions are critical points of the entropy functional S_D with constraint on the sum of bulk and surface internal energy (21) and constraints (29) on the number of molecules of the mixture assuming the quantities Z_{JD} are fixed. Thus, equilibrium states of the mixture must satisfy the variational equation, which generalizes Eq. 23

$$\delta S_D - \lambda_0 \delta U_D - \lambda_J \delta Z_{JD} = 0, \tag{30}$$

where λ_0 and λ_J are Lagrangian multipliers. After substitution of expression (8) into Eq. 30, the new equation is obtained instead of Eq. 26

$$\Theta_i = \lambda_J \zeta_{Ji}. \tag{31}$$

Notwithstanding the fact that coefficients ζ_{Ji} are defined non-uniquely, Eq. 31 is formulated quite uniquely. Any transformation $\zeta_{Ji} \to \zeta'_{Ji} = \alpha_{JJ'} \zeta_{J'i}$ with a square non-degenerate matrix $\alpha_{JJ'}$ of dimension K_1 corresponds to the transformation of Lagrangian multipliers $\lambda_J \to \lambda'_J = \beta_{JJ'} \lambda_{J'i}$, where $\beta_{JJ'}$ is the inverse matrix to the matrix $\alpha_{JJ'}$. Note that in the absence of chemical reactions, $K = 0$ and a square matrix ζ_{Ji} can be selected as unity matrix $\zeta_{Ji} = \delta_{Ji}$. Therefore, the system of Eq. 31 is reduced to Eq. 26. Thus, Eq. 31 generalizes Eq. 26. If two or several phases are present in an equilibrium state, then far from the interfacial regions, these phases can be considered practically homogeneous, so system of Eq. 31 provides for the equality of chemical potentials for each chemical component in every phase. In this way, the developed theory complies with the classical thermodynamics [2, 47].

It follows from the identity (20) and Eqs. 18, 25, and 31 that for equilibrium states, the following equations are satisfied

$$\partial_b \sigma_{ab} = 0, \tag{32}$$

which should be interpreted as conditions for mechanical equilibrium of the mixture.

Let us now turn to hydrodynamic processes without chemical reactions and external sources described in the frame of the theory with entropy functional (7). The motion of a mixture obeys conservation laws for chemical components, momentum, and energy [52]. In the Cartesian coordinate system, these laws can be presented in the form of the following equations

$$\partial_t n_i + \partial_a (n_i v_a + Q_{ia}) = 0, \tag{33}$$
$$\partial_t (\rho v_a) + \partial_b (\rho v_a v_b - p_{ab}) = 0, \tag{34}$$
$$\partial_t \varepsilon + \partial_a (\varepsilon v_a + q_a + p_{ba} v_b) = 0. \tag{35}$$

Here, we introduce symmetric stress tensor p_{ab}, diffusion flux vector Q_{ia}, and heat flux vector q_a. By definition, the diffusion flux satisfies the constraint

$$m_i Q_{ia} = 0. \tag{36}$$

The hydrodynamic problem (33–35) is not yet closed. To close the Cauchy problem in Eqs. 33–35, it is necessary to specify boundary conditions and constitutive relations, i.e., explicit expressions for Q_{ia}, p_{ab}, and q_a. We introduce no-slip boundary condition at a contact with solid

$$v_a \mid_{\partial \mathrm{D}} = 0 \tag{37}$$

and the condition of impermeability for the diffusion flux (l_a is the internal normal unit vector at the boundary ∂D)

$$l_a Q_{ia} \mid_{\partial \mathrm{D}} = 0. \tag{38}$$

There can be other boundary conditions directly associated with particular model entropy functionals; those will be discussed below.

The constitutive relations characterize internal rheological and dissipative properties of the system. They should provide a non-negative contribution to the entropy production. This requirement helps us to derive the constitutive relations (but not in a unique way). In order to calculate the contribution of various processes to entropy production, we use Eq. 8, in which we substitute the expressions for time derivatives of densities of components and internal energy using Eqs. 33–35. After integrating by parts with account for Eqs. 37 and 38, we obtain

$$\frac{dS_D}{dt} = \Sigma_{int} + \Sigma_b, \tag{39}$$
$$\Sigma_{int} = \int_D \sigma_{int} dV, \tag{40}$$
$$\Sigma_b = \int_{\partial D} \Theta_0 q_a l_a dA + \Gamma_u [\partial_t u] + \Gamma_i [\partial_t n_i], \tag{41}$$
$$\sigma_{int} = (\Theta_0 p_{ab} - \Sigma_{ab}) \partial_b v_a + q_a \partial_a \Theta_0 + Q_{ia} \partial_a \Theta_i, \tag{42}$$

In Eq. 39, the term Σ_{int} describes the entropy change rate caused by internal processes, i.e., the *entropy production*, and the term Σ_b describes the entropy changes caused by boundary effects (for example, heat inflow at the boundary). The quantity σ_{int} characterizes entropy production per unit volume. The analysis of expression (42) makes it possible to identify the tensor $\sigma_{ab} = T_S \Sigma_{ab}$ with the tensor of static stresses in the mixture, i.e., with the part of the total stress tensor p_{ab}, which does not depend on velocity gradient and gives no contribution to the entropy production. The contribution to entropy production from internal stresses is caused by the tensor $\tau_{ab} = p_{ab} - \sigma_{ab}$, which is referred to as the viscous stress tensor. Since the entropy production must be non-negative, we will formulate the constitutive relations in accordance with two inequalities

$$q_a \partial_a \Theta_0 + Q_{ia} \partial_a \Theta_i \geq 0, \tag{43}$$
$$\tau_{ab} \partial_b v_a \geq 0. \tag{44}$$

To formulate the constitutive relations for the heat flux q_a and diffusion fluxes Q_{ia} in a compact form, it is convenient to denote $Q_{0a} = q_a$ and introduce indices A and $B = 0, 1, \ldots M$. Then the inequality (43) can be rewritten in a simple form $Q_{Aa} \partial_a \Theta_A \geq 0$, which is satisfied by the following constitutive relations

$$Q_{Aa} = \mu_{AB} \partial_a \Theta_B. \tag{45}$$

Here, in accordance with Onsager's theory [5], the matrix μ_{AB} must be symmetric with non-negative eigenvalues. Only one zero eigenvalue exists that is related to the condition (36)

$$m_i \mu_{iB} = 0. \tag{46}$$

The constitutive relations (45) are interpreted as the generalized Fourier-Fick law. Let us turn now to the inequality (44), which puts a restriction on the possible type of relation between the viscous stress tensor τ_{ab} and the strain rate tensor $e_{ab} = 2^{-1}(\partial_a v_b + \partial_b v_a)$. To formulate the possible

types of such relation, it is convenient to subdivide τ_{ab} and e_{ab} into spherical and deviator terms

$$\tau_{ab} = \tau^v \delta_{ab} + \tau^s_{ab}, \quad \tau^v = \tau_{aa}/3, \quad \tau^s_{ab} = \tau_{ab} - \tau^v \delta_{ab} \quad \text{and} \tag{47}$$

$$e_{ab} = e^v \delta_{ab} + e^s_{ab}, \quad e^v = e_{aa}/3, \quad e^s_{ab} = e_{ab} - e^v \delta_{ab}. \tag{48}$$

Inequality (44) is satisfied by the following constitutive relations, which establish the dependence between τ^v, e^v and τ^s_{ab}, e^s_{ab} respectively

$$\tau^v = k_v \left(\left| \tau^v \right| \right) e^v, \tag{49}$$

$$\tau^s_{ab} = k_s \left(\tau^s \right) e^s_{ab}, \quad \tau^s = (\tau^s_{ab} \tau^s_{ab})^{1/2}, \tag{50}$$

where k_v and k_s are non-negative functions. In the special case when $k_v = \eta_v$ and $k_s = \eta_s$ are coefficients of volume and shear viscosity, respectively, we obtain the well-known linear viscous Newtonian model

$$\tau_{ab} = \left(\eta_v - \frac{2}{3}\eta_s \right) e_{cc} \delta_{ab} + 2\eta_s e_{ab}. \tag{51}$$

Now let us consider the hydrodynamics of mixtures with chemical reactions. The motion of a mixture obeys the hydrodynamic Eqs. 34 and 35 for momentum and energy of the mixture and the modified equation for the molar densities of components (instead of Eq. 33)

$$\partial_t n_i + \partial_a (n_i v_a + Q_{ia}) = h_I \eta_{Ii} \tag{52}$$

where h_I is the intensity of chemical reaction with the number I.

In much the same way as previously, it is possible to derive the entropy production rate per unit volume (compare with Eq. 42)

$$\sigma_{int} = (\Theta_0 p_{ab} - \Sigma_{ab}) \partial_b v_a + q_a \partial_a \Theta_0 + Q_{ia} \partial_a \Theta_i + h_I \eta_{Ii} \Theta_i \tag{53}$$

Thus, for a mixture with chemical reactions, additional constitutive relations are required for the quantities h_I, which determine the chemical reactions kinetics. All the considerations with respect to the heat flux q_a, diffusion fluxes Q_{ia}, and the stress tensor p_{ab} presented previously remain in force. For the quantities h_I, it is sufficient to satisfy the inequality

$$h_I \eta_{I\,i} \Theta_i \geq 0 \tag{54}$$

This can be achieved using the expression for reaction kinetic terms as follows

$$h_I = X_I(\upsilon'_{Ii} \Theta_i) - X_I(\upsilon_{Ii} \Theta_i) \tag{55}$$

In the right-hand part of Eq. 55, there is no summation over I and $X_I = X_I(\psi)$ is a monotonically decreasing function. In a particular case of the Arrhenius kinetic law, there is the explicit expression $X_I(\psi) = X_{I0} \exp\left(-\frac{\psi}{R}\right)$, where R is the universal gas constant and X_{I0} is a positive temperature-dependent coefficient.

The constitutive relations (45), (49), (50), and (54) close the hydrodynamic problem in the sense that the number of unknowns becomes equal to the number of equations. Of course, it is implied that the coefficients or functions entering into these relations are explicitly given in an analytical of tabular form. Also, it is worth to repeat that these relations are sufficient for non-negative entropy production, but *not necessary*. This means that there can be more complex diffusion, rheology, or chemical kinetics, which is consistent with non-negative entropy production.

There are many instances when hydrodynamic processes can be described in isothermal approximation. The isothermal problem formulation for multicomponent mixtures can be obtained from the non-isothermal formulation just by dropping the energy Eq. 35 and assuming the condition $T_S = \text{const}$.

However, because the scope of isothermal problems is very wide, it is useful to have independent exposition of DFT approach just for these problems. The chemical reactions are assumed to be absent. Instead of the entropy functional, one has to use the Helmholtz energy functional, which depends on the fields of molar densities of chemical components

$$F_D = F_D[n_i]. \tag{56}$$

The dependence on temperature is not shown explicitly here and further in other equations for isothermal problems. The functional (56) can be obtained from the relationship between Helmholtz energy, internal energy, and entropy

$$F_D = U_D - T_S S_D, \tag{57}$$

The properties of the functional (57) depend on properties of the entropy functional (7). At the same time, since Helmholtz energy is used for isothermal processes, the number of main properties is considerably less than in the case of the entropy.

Helmholtz energy property 1 The Helmholtz energy functional (56) is supposed to be continuous and differentiable at a suitable convex set in linear functional space of the fields of component molar densities.

In accordance with this property, the variation of the Helmholtz free energy functional in the general case has the form

$$\delta F_D = \int_D \Phi_i \delta n_i dV + \tilde{\Gamma}_n[\delta n_i] \tag{58}$$

where variational derivatives are used

$$\Phi_i = \frac{\delta F_D}{\delta n_i} \tag{59}$$

and the term $\widetilde{\Gamma}_n$ denotes linear boundary operator acting on variations δn_i. The explicit expressions for boundary operators $\widetilde{\Gamma}_n$ are dependent on the explicit form of the Helmholtz energy functional and will be discussed below.

Helmholtz energy property 2 In a particular case, when

(a) The boundary of the domain under consideration ∂Dcoincides with a solid surface that is uniform in terms of its properties
(b) The values of n_i are constants (i.e., the state of the mixture is homogeneous)

then the Helmholtz energy functional F_D is reduced to the expression

$$F_D = fV_D + f_* A_{\partial D}, \tag{60}$$

where $f = u - Ts$ is the Helmholtz energy density in the conventional equilibrium thermodynamics, $f_* = u_* - Ts_*$ is the surface density of Helmholtz energy associated with the boundary between the mixture and the solid surface, and $A_{\partial D}$ is the area of this boundary.

Helmholtz energy property 3 Functional (56) can be rewritten in a curvilinear coordinate system y^a as the functional of molar densities of chemical components of the mixture $n_i(t, y^a)$ and the metric tensor of the curvilinear coordinate system $g_{ab}(y^c) = \frac{\partial x^d}{\partial y^a} \times \frac{\partial x^d}{\partial y^b}$, as follows:

$$F_D = F_D[n_i, g_{ab}], \tag{61}$$

and the functional (61) is invariant with respect to any transformation of coordinates.

Calculating the variation of the functional (61), it is possible to derive the extended version of Eq. 58

$$\delta F_D = \int\limits_D (\Phi_i \delta n_i + 2^{-1}\sigma^{ab}\delta g_{ab}) g^{1/2} dy^1 dy^2 dy^3 + \widetilde{\Gamma}_n[\delta n_i] + \widetilde{\Gamma}_g[\delta g_{ab}], \tag{62}$$

where $\widetilde{\Gamma}_g$ is the boundary operator acting on the variation of the metric and the set of values σ^{ab} is associated with the variational derivative of Helmholtz free energy with respect to the metric

$$\sigma^{ab} = 2\frac{\delta F_D}{\delta g_{ab}} \tag{63}$$

The definition (63) of the static stress tensor σ^{ab} is consistent with Eq. 18. The postulated invariance of Eq. 61 with respect to transformation of coordinates (see Helmholtz energy property 3 above) makes it possible to use the Noether's theorem for deriving the differential identity bridging the variational derivatives Φ_i and σ_{ab} [24, 33]. In a curvilinear coordinate system, this identity has the form

$$\nabla_b \sigma^{ab} = -g^{ab} g^{-1/2} n_i \partial_b (g^{1/2} \Phi_i), \tag{64}$$

where ∇_a is the operator of covariant derivative [54].

In the Cartesian coordinate system identity (64) is simplified

$$\partial_b \sigma_{ab} = -n_i \partial_a \Phi_i. \tag{65}$$

In equilibrium states, Eq. 26 actually means that quantities (59) are constants, and we again arrive to the equations of mechanical equilibrium (32).

In isothermal problems, there exists the dissipative condition, which is similar to the condition of non-negative entropy production. Namely, when there are no external forces in bulk or at the boundary, the total energy, which is composed of kinetic energy and Helmholtz energy (56), should decrease. Performing direct calculations with account of Eqs. 33, 34, 37, and 38, it is possible to find the expression for the total energy change rate

$$\frac{dE}{dt} = \widetilde{\Sigma}_{int} + \widetilde{\Sigma}_b, \tag{66}$$

$$E = \frac{1}{2}\int\limits_D \rho v_a v_a dV + F_D,\ \widetilde{\Sigma}_{int} = \int\limits_D \chi_{int} dV,\ \widetilde{\Sigma}_b = \widetilde{\Gamma}_i[\partial_t n_i] \tag{67}$$

$$\chi_{\text{int}} = Q_{ia}\partial_a \Phi_i - \tau_{ab}\partial_a v_b. \tag{68}$$

Evidently, the term $\widetilde{\Sigma}_{int}$ describes the dissipation of energy in the bulk, while the term $\widetilde{\Sigma}_b$ describes boundary effects. For the consistency with dissipative condition, it is necessary to satisfy two inequalities, one of which is Eq. 44 and another is the following:

$$Q_{ia}\partial_a \Phi_i \le 0. \tag{69}$$

We have already discussed how to satisfy inequality (44) (see Eqs. 47–51). Inequality (69) can be satisfied by the following constitutive relations for diffusion fluxes

$$Q_{ia} = -D_{ij}\partial_a \Phi_j, \tag{70}$$

where D_{ij} is a symmetrical non-negative matrix, which has one eigenvector with the zero eigenvalue

$$D_{ij} m_j = 0. \tag{71}$$

Comparison with Eq. 45 makes it possible to make the identification

$$D_{ij} = T_S^{-1}\mu_{ij}. \tag{72}$$

Now we have introduced the constitutive relations, which make the hydrodynamic problem closed and consistent with thermodynamics. These additional relations contain rheological and transport parameters, which should be specified in every particular case. Usually they are measured experimentally for the considered mixtures or calculated with the help of semiempirical correlations. Though the general mathematical structure of the density functional hydrodynamics is developed, one has to specify the functional of entropy or Helmholtz energy explicitly to apply to this theory. This is done in the next section.

3 Basic DFT hydrodynamic model

The simplest way to take account of entropy associated with inhomogeneous parts of the mixture is to introduce terms dependent on gradients of component molar densities

$$S_D = S_D[u, n_i] = \int_D (s(u, n_i) - 2^{-1}\alpha_{ij}(n_k)\partial_a n_i \partial_a n_j) dV + \int_{\partial D} s_*(u, n_i) dA \quad (73)$$

Having expression Eq. 73, it is possible to find explicit expressions for all quantities, which were discussed in Secttion 2, in a straightforward way:

$$S_D = S_D[u, n_i, g_{ab}] = \int_D \Omega dV + \int_{\partial D} \Omega_* dA \quad (74)$$

$$\Omega = s(u\,|g|^{-1/2}, n_i\,|g|^{-1/2}) - 2^{-1} g^{ab}\alpha_{ij}(n_k\,|g|^{-1/2})\partial_a(n_i\,|g|^{-1/2})\partial_a(n_j\,|g|^{-1/2}) \quad (75)$$

$$\Omega_* = s_*(u\,|g|^{-1/2}, n_i\,|g|^{-1/2}) \quad (76)$$

$$\Theta_i = -T^{-1}\kappa_i - 2^{-1}\alpha_{jk,i}\partial_a n_j \partial_a n_k + \partial_a(\alpha_{ij}\partial_a n_j), \quad (77)$$

$$\Sigma_{ab} = (-T^{-1}(p - \kappa_i n_i) + 2^{-1}\alpha_{ij}\partial_a n_i \partial_a n_j + \Theta_i n_i)\delta_{ab} - \alpha_{ij}\partial_a n_i \partial_b n_j, \quad (78)$$

$$\Gamma_u = \int_{\partial D} s_{*,u}\delta u, \quad \Gamma_i = \int_{\partial D} (s_{*,i} + \alpha_{ij} l_a \partial_a n_j)\delta n_i dA, \quad (79)$$

where l_a is the internal unit normal vector to the surface ∂D. Note that elementary volume dV and surface area dA in Eq. 74 are implicitly dependent on metric tensor g_{ab}, because they are calculated in curvilinear coordinates. Also, it is useful to write down quantities, which are related to Helmholtz energy functional:

$$F_D = F_D[n_i] = \int_D (f(n_i) + 2^{-1}\nu_{ij}(n_k)\partial_a n_i \partial_a n_j) dV + \int_{\partial D} f_*(n_i) dA \quad (80)$$

$$\Phi_i = \kappa_i + 2^{-1}\nu_{jk,i}\partial_a n_j \partial_a n_k - \partial_a(\nu_{ij}\partial_a n_j), \quad (81)$$

$$\sigma_{ab} = (f + 2^{-1}\nu_{ij}\partial_a n_i \partial_a n_j - \Phi_i n_i)\delta_{ab} - \nu_{ij}\partial_a n_i \partial_b n_j, \quad (82)$$

where $\nu_{ij} = T_S\alpha_{ij}$. All requirements from Section 2 for entropy functional and Helmholtz energy functional are satisfied. They can be checked directly or follow from the properties of equilibrium thermodynamic functions, which are used in definitions (73) and (80). The explicit expressions for boundary terms (79) make it possible to find additional boundary conditions. They must be consistent with Eq. 24 for equilibrium states. We introduce boundary conditions for the densities

$$\nu_{ij} l_a \partial_a n_j = f_{*,i} \quad (83)$$

Also in non-isothermal problems, it is necessary to specify temperature or heat flux at the boundary. The explicit form for the static stress tensor makes it possible to find the expression for interfacial tension coefficient in case of two-phase states. Indeed, let us consider the equilibrium state with all parameters dependent on only one coordinate x^1. Let us assume that at $x^1 \to -\infty$ the densities n_i converge to the densities n_{iA} of phase A, and at $x^1 \to +\infty$ they converge to the densities n_{iB} of phase B. Since the quantities (81) are constant in equilibrium, we derive the equilibrium condition for chemical potentials

$$\kappa_i(n_{jA}) = \kappa_i(n_{jB}) \quad (84)$$

Besides, we get from the Eq. 32 a very simple equation $\partial_1\sigma_{11} = 0$, which proves the equality of pressures in phases A and B

$$p(n_{jA}) = p(n_{jB}) \quad (85)$$

Then one calculates the interfacial tension between phases A and B

$$\gamma_{AB} = \int_{-\infty}^{+\infty} (\sigma_{22} - \sigma_{11}) dx^1 = \int_{-\infty}^{+\infty} \nu_{ij}(n_k)\partial_1 n_i \partial_1 n_j dx^1 \quad (86)$$

By more detailed consideration it is possible to prove the Laplace equation for capillary pressure jump in case of curved interfacial surfaces [11].

4 Advanced DFT models

Advanced DFT models use more complex density functional expressions in order to describe the phenomena, which lie outside the basic model. In particular, some phenomena would require non-local and non-linear operations for the computation of density functional. Here, we describe the extension of the basic model with a possibility to describe elastic bodies (or elastic phases) alongside with fluid phases. In order to introduce elasticity in hydrodynamics, it is necessary to introduce strain tensor. We rely on the ideas of the continuous defect theory [6, 28, 29, 37–39, 43], which treat the strain tensor as an individual primary quantity with separate dynamic equation. This strain tensor does not necessarily satisfy the compatibility conditions, because of the possible presence of continuously distributed defects. In non-linear theory, there are different strain tensors; here, we assume the Almansi strain tensor ε_{ab} [21, 34, 41, 44, 58]

as primary quantity. In addition to usual Eqs. 33–35, one has the equations for the strain tensor ε_{ab}

$$\partial_t \varepsilon_{ab} = 2^{-1}(\partial_b v_a + \partial_a v_b) - \varepsilon_{cb}\partial_a v_c - \varepsilon_{ac}\partial_b v_c - v_c \partial_c \varepsilon_{ab} - \omega_{ab} \tag{87}$$

Here, the quantities ω_{ab} are related to possible defects. In case of classical elasticity theory, these quantities are identically zero. In general case, they must be specified in accordance with non-negative entropy production requirement.

For the problems with elastic phases, we use entropy functional (73) with additional condition that internal energy and entropy of a deformable solid depend on temperature T, molar densities n_i, and the strain tensor ε_{ab}:

$$u = u(T, n_i, \varepsilon_{ab}), \quad s = s(T, n_i, \varepsilon_{ab}) \tag{88}$$

Using this with auxiliary parameters $\chi_{ab} = \left(\frac{\partial u}{\partial \varepsilon_{ab}}\right)_{s,n_i}$, one can recalculate the entropy production term (42) and the static stress tensor (82) with the following results:

$$\sigma_{int} = T^{-1}\tau_{ab}\partial_b v_a + q_a \partial_a \Theta_0 + Q_{ia}\partial_a \Theta_i + T^{-1}\omega_{ab}\chi_{ab}, \tag{89}$$

$$\sigma_{ab} = (f + 2^{-1}\nu_{ij}\partial_a n_i \partial_a n_j - \Phi_i n_i)\delta_{ab} - \nu_{ij}\partial_a n_i \partial_b n_j + \chi_{ab} - \chi_{ac}\varepsilon_{bc} - \chi_{bc}\varepsilon_{ac}. \tag{90}$$

Thus, we have an additional condition for non-negative entropy production

$$\omega_{ab}\chi_{ab} \geq 0 \tag{91}$$

It is easy to verify that this inequality is satisfied by the following constitutive relations

$$\omega_{ab} = \alpha_v \delta_{ab}\chi_{cc} + \alpha_s \left(\chi_{ab} - \frac{1}{3}\delta_{ab}\chi_{cc}\right) \tag{92}$$

where α_v and α_s non-negative kinetic coefficients (relaxation parameters of volume and shear strains, respectively). Of course, in numerical modeling or practical applications, parameters α_v and α_s must be explicitly specified as well as function (88) and other relevant parameters (see Section 3). This is done by using experimental data or semiempirical expressions.

5 Numerical simulator

The system of equations described in Section 2 and given by Eqs. 33–34 jointly with the necessary constitutive relations and boundary conditions (Sections 2–4) represents a rather complex mathematical problem. This problem differs significantly from the problems known in other multiphase flow modeling techniques. Indeed, Eqs. 33–34 are highly non-linear. They involve Helmholtz energy or entropy density and its derivatives. The particular expressions for these functions come from thermodynamics and usually contain polynomial rational functions and logarithms. Besides being non-linear, Eqs. 33–34 are complicated by the higher order spatial derivatives—to the fourth order. The scope of the difficulties demands usage of new unconventional numerical methods. Historically, we began numerical simulations using an explicit first-order in space and time method [7, 8] that was a development from the large-particle class of methods [4]. In the later simulations, we focused on a more advanced explicit second-order in space first-order in time method, which we developed following the ideas described in [46]. Our conservative finite-volume method uses Cartesian uniform staggered grid, on which scalar quantities and diagonal tensor components are ascribed to the centers of cells, vector components are ascribed to the centers of cell sides, and off-diagonal tensor components are ascribed to the centers of cell edges. Our method, called tensor-aligned conservative uniform symmetric (TACUS) [9], allows for efficient parallelization and implementation on the modern computer clusters. In 2005, we developed a research code called direct hydrodynamic (DHD) simulator, which solves the DFH equations numerically using the TACUS method. Later, the simulator was parallelized and optimized, and now it runs on the multicore CPU or GPGPU clusters. Depending on the physics of a multiphase problem, the typical scenarios can be simulated on models with sizes from 200^3 cells (using several GPGPU cards) to 1000^3 and more cells (using a 64-GPGPU computer cluster) within a day.

6 Basic numerical solutions

In this section, we show numerical simulation of several relatively simple problems to demonstrate modeling of particular fundamental multiphase phenomena such as capillary pressure, contact angles, moving contact line, interfacial topological changes, dynamic effects and surfactantrelated phenomena. Historically, we used such problems for validation of our numerical simulator, DHD. The comprehensive validation is summed up in our book [9], while particular validation examples can be found in our papers [7, 8, 10, 16–19] In Sections 6.1–6.3 we obtain numerical solutions of governing Eqs. 33 and 34 with constitutive relations (51), (70), (81), and (82) and boundary conditions (37), (38), and (83). In Section 6.4 we use additional governing Eq. 87. The interfacial tension γ is related to the coefficients ν_{ij} by Eq. 86. Assuming γ is known from experiment, Eq. 86 is solved numerically to find parameters ν_{ij}. The construction of Helmholtz energy functions f and f_* is the domain of chemical thermodynamics; for this kind of problems, it is described in [9, 10].

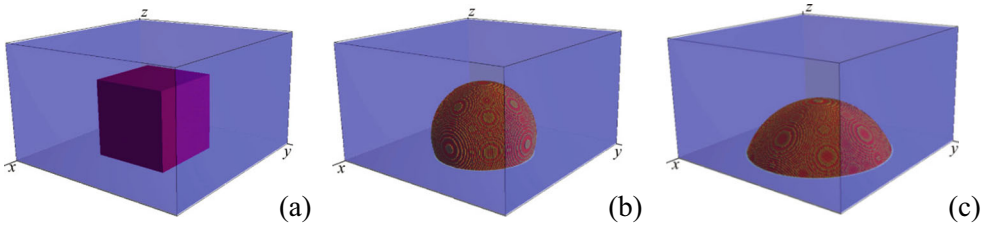

Fig. 1 Sessile drop problem. 3D view of component 1 concentration in initial conditions (**a**) and equilibrium solution in case 1 (**b**) and case 2 (**c**); phase A is shown in *red* and phase B in *semitransparent blue*, and *other colors* indicate the transition zone

6.1 Sessile drop

We start from a simple two-phase problem of an equilibrium sessile drop. Let a drop of one liquid (phase B) be immersed in a bulk of another liquid (phase A), and the drop touches a flat solid surface. In this case, the drop forms a contact angle, whose value depends on the wetting properties (wettability) of the surface and on the interfacial tension (IFT) or capillary pressure between the two liquid phases. In the absence of gravity, the contact angle is calculated using the well-known Young equation [40]:

$$\cos\theta = \frac{\gamma_A - \gamma_B}{\gamma_{AB}}, \tag{93}$$

where γ_{AB} is the IFT between phases A and B, γ_A and γ_B are the IFTs between the solid and phases A and B, respectively, and θ is the contact angle.

In extreme cases when $|\gamma_A - \gamma_B| \geq \gamma_{AB}$, the drop either spreads over the solid surface ($\gamma_A - \gamma_B > 0, \theta = 0°$) or completely detaches ($\gamma_A - \gamma_B < 0, \theta = 180°$).

As an example, we will consider two cases, one of which is that a drop forms an obtuse contact angle and in the other case, an acute one.

The simulation is conducted within a model, which is a parallelepiped with the dimensions 0.01 m ×0.01 m ×0.006 m along the $x-$, $y-$, and z-axes, respectively. The model is approximated by 200 ×200 ×120 cubic cells. The IFT between phases A and B is $\gamma_{AB} = 0.056$N/m. The mixture contains two chemical components and the equilibrium phase A consists 100 % of the component 1, while the equilibrium phase B consists 100 % of the component 2.

In both cases, the boundary conditions are impermeable walls on either side of the model. At one of the walls—the bottom one at $z = 0$ m—the surface wettability is determined by the condition $\gamma_A - \gamma_B = -0.025$ N/m for case 1 or $\gamma_A - \gamma_B = 0.025$ N/m for case 2. At all the other walls, the condition $\gamma_A - \gamma_B = 0$ N/m is specified in both cases.

The initial conditions are identical in both cases. The model is filled with phase A everywhere except a place near the center of the bottom wall, where a fragment of phase B is specified. This fragment is a cube with the edge size of 0.004 m (Fig. 1a).

Obviously, the initial conditions just described are non-equilibrium with respect to the acting surface forces. Therefore, once numerical simulation is started, the system begins evolving towards the equilibrium configuration. Figure 1b, c shows the achieved equilibrium distribution of phases in cases 1 and 2, respectively. The equilibrium contact angles can be measured conveniently using the distribution of phases as they appear within a 2D section passing through the drop axis of symmetry as shown in Fig. 2; measurement accuracy is determined by grid resolution. The contact angles given by (90) are $\theta_1 \cong 117°$in case 1 and $\theta_2 \cong 63°$ in case 2. The values, measured using Fig. 2, are very close to the expected ones within 3.5 % tolerance.

Concluding the sessile drop discussion, we note that although this simple numerical simulation example validates consistency between IFTs (or capillary pressure) and

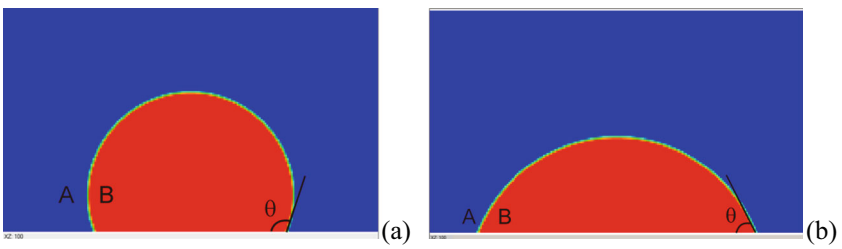

Fig. 2 Sessile drop problem. Equilibrium component 1 concentration in case 1 (**a**) and case 2 (**b**) shown within 2D section passing through the coordinate $y = 0.005$ m parallel xz-plane; phase A is shown in *red* and phase B in *semitransparent blue*, and *other colors* indicate the transition zone

contact angles, it also demonstrate modeling of such an important phenomenon as moving contact line. Indeed, the contact line motion is the necessary mechanism involved in bringing the system from the initial state shown in Fig. 1a to one of the equilibrium states shown in Fig. 1b, c.

6.2 Sessile drop in the presence of surfactant

In one of our previous papers [19], we have explained how surfactant-related phenomena can be modeled by DFH. Those well-known phenomena are as follows [50]:

- Accumulation of surfactant inside interfacial area with simultaneous reduction of IFT
- Gibbs effect—an apparent increase in IFT when the interface surface is stretched
- Marangoni effect—the local flow and mass transfer along an interface driven by an IFT gradient

Here, we demonstrate how the sessile drop from Sect. 6.1 is changed under the influence of surfactant dissolved in one of the phases. We model two mechanisms:

- Surfactant accumulation inside of an interfacial region between two liquid phases and simultaneous reduction of IFT
- Surfactant adsorption on a liquid-solid contact and simultaneous reduction of IFT

Note that generally, the presence of one of the mechanisms does not exclude the possibility of the other mechanism, because a mixture may contain several surfactants acting in different ways.

Modeling of the said surfactant mechanisms is possible in the following way. In the DFH, it is necessary to specify dependence between the surfactant local molar density and the coefficient v_{ij} in Eq. 80. Analogy with the Langmuir isotherm [50] leads to the following relation:

$$v_{ij} = \left(v_0 + \frac{\Delta v}{1 + a_\mathrm{s} n_\mathrm{s}} \right) \delta_{ij}, \tag{94}$$

with positive model parameters $v_0, \Delta v$, and a_s. Coefficients v_0 and Δv are selected numerically to ensure that a given IFT value γ_0 in the absence of surfactant is held and that it never goes below the specified $\gamma_{\min}$ in the presence of surfactant. The coefficient a_s characterizes the influence of surfactant adsorption on the IFT reduction. This coefficient is also selected numerically to have a specified IFT value γ_1 when the surfactant surface density inside an interface is $n_{\mathrm{s}1}^{\mathrm{srf}}$; this surface density corresponds to a particular surfactant bulk molar density $n_{\mathrm{s}1}$ in one of the phases. The described approach is suitable for modeling surfactant acting on a liquid-liquid interface.

To model surfactant acting on a liquid-solid interface, it is necessary to introduce Helmholtz energy surface density dependence on the surfactant local molar density:

$$f_* = \xi_{1i} n_i + (\xi'_{1i} n_i) \psi_\mathrm{s}(n_\mathrm{s}) + \xi_0, \tag{95}$$

where n_s is the surfactant molar density and $0 \le \psi_\mathrm{s}(n_\mathrm{s}) \le 1$ is the surfactant adsorption function that is determined by the particular surfactant properties. The coefficients $\xi'_{1i}, \quad i = 1, .., M$ describe surfactant-induced influence on IFT in the presence of particular mixture components, and ξ_0 is the irreducible surface energy, which does not influence the solution. The unknown coefficients, $\xi'_{1i}, \quad i = 1, .., M$ and ξ_0 satisfy the following system of linear algebraic equations:

$$\xi_{1i} n_{im} + (\xi'_{1i} n_{im}) + \xi_0 = f'_{*m}, \quad m = 1, ..., M_\mathrm{ph} \tag{96}$$

where f'_{*_m} are the given liquid-solid IFT values (the Helmholtz energy surface density) for the mth phase corresponding to $\psi_\mathrm{s}(n_\mathrm{s}) = 1$ (i.e., at maximum surfactant adsorption), n_{im} and $n_{\mathrm{s}m}$ are molar densities of the ith mixture component and surfactant, respectively, in the mth phase, and M_ph is the number of phases possible in the mixture. The function $\psi_\mathrm{s}(n_\mathrm{s})$ has the form as follows:

$$\psi_\mathrm{s}(n_\mathrm{s}) = \frac{\beta_\mathrm{s} n_\mathrm{s}}{1 + \beta_\mathrm{s} n_\mathrm{s}}, \tag{97}$$

where β_s is the auxiliary positive model coefficient. The function $\psi_\mathrm{s}(n_\mathrm{s})$ in Eq. 97 describes the classical behavior of a surfactant, which is a rapid initial growth of adsorption followed by a slower adsorption when surfactant surface concentration approaches saturation. The coefficient β_s is selected numerically to have a given liquid-solid IFT value γ_s at the surfactant surface density $n_{\mathrm{s}1}^{\mathrm{srf}}$.

In case of surfactant, the bulk Helmholtz energy includes additional terms to ensure specific solubility of the surfactant in phases. The examples can be found in [10, 19].

We begin by modeling surfactant acting on a liquid-liquid interface. Let us recall the sessile drop problem statement from Section 6.1. Here, we use the same model geometry and the same two liquid phases. We add an additional chemical component, a surfactant, with the following relevant properties: $\gamma_{\mathrm{AB\ min}} = 0.035$ N/m, $\gamma_{AB\,1} = 0.037$ N/m, $n_{\mathrm{s}1}^{\mathrm{srf}} = 3.7 \cdot 10^{-9}$ kmol/m^2, and $n_{\mathrm{s}1} = 2.1 \times 10^{-9}$ kmol/m^3. The surfactant is dissolvable in both phases. The model coefficients $v_0, \ \Delta v, \ $ and a_s were selected to ensure surfactant's action with the said properties.

We demonstrate surfactant modeling using case 2 from Sect. 6.1, which is specified by liquid-solid IFTs such that $\gamma_\mathrm{A} - \gamma_\mathrm{B} = 0.025$ N/m corresponding to the contact angle $\theta_2 \cong 63^\circ$ in the absence of surfactant. We assume the initial conditions to be the steady-state solution of the original sessile drop problem (Figs. 1c and 2b). We add the third chemical component, the surfactant, distributed uniformly

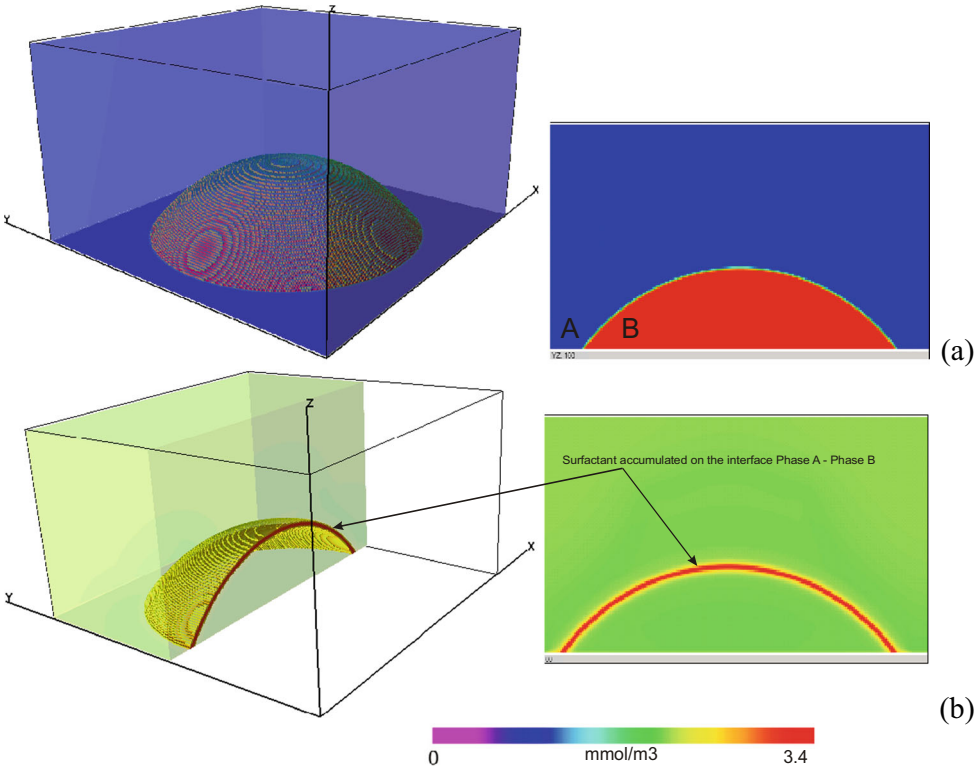

Fig. 3 The sessile drop in the presence of surfactant acting on the liquid-liquid interface. **a** Steady-state distribution of component 1 concentration in the presence of a surfactant; **b** steady-state distribution of the surfactant molar density. The *left-hand column* shows 3D views of the model, while the *right-hand column* shows the 2D view inside of the section passing through $y = 0.005$ m parallel to the *xz*-plane. In (**a**), phase A is shown in *semitransparent blue*, phase B in *red*, and the *other colors* indicate the transition zone. In (**b**), the *left-hand image* shows half of the 3D view with the portion of the model at $0\,\text{m} \le y \le 0.005\,\text{m}$ removed from view; the colors correspond to the color palette with the range $n_s \le 1.9$ mmol/m^3 being semitransparent in the 3D view

with molar density $n_s = 1.7 \times 10^{-6}$ kmol/m^3. The presence of the surfactant makes the state of the two-phase system non-equilibrium.

The new equilibrium solution found by perfuming numerical simulation is presented in Fig. 3. During the evolution of the system, the surfactant has partially accumulated inside of the interfacial area between phases A and B (Fig. 3b). Due to the IFT reduction, the contact angle has changed. In particular, the new contact angle measured using the 2D section of Fig. 3a appears to be close to 45°. The theoretical value for the angle is obtainable from Eq. 93 by using the known values of $\gamma_A - \gamma_B$ and $\gamma_{AB\ min}$; it is 44°, which gives very good correspondence to the numerical result.

Now let us turn to modeling the second mechanism, when a surfactant acts on the liquid-solid interface. The modeling parameters are as follows: $\gamma_{As} = 0.013$ N/m and $n_s^{srf} = 3.5 \times 10^{-9}$ kmol/m^2. The surfactant is dissolvable in the ambient phase A only. The liquid-solid IFT for phase B, γ_{Bs}, is not affected by the surfactant. The required surfactant model parameters were found by solving the linear algebraic system (96) and by selecting numerically the coefficient β_s in Eq. 97. Using the conditions of the same case 2, we have for the liquid-solid IFTs at the maximum surfactant adsorption the following relation $\gamma_{As} - \gamma_B = 0.013$ N/m (at $\gamma_B = 0$ N/m).

Again, the steady-state solution for case 2 (Section 6.1) is taken as initial conditions for the distribution of the first two chemical components. The third chemical component (surfactant) is distributed uniformly with molar density, $n_s = 1.9 \times 10^{-6}$ kmol/m^3, in the entire bulk of the model. The new steady-state solution was found by performing the numerical simulation. During the evolution of the system, the surfactant was gradually adsorbed into the boundary between phase A and the solid wall of the model; the residual surfactant has migrated into phase A. The process was accompanied by a simultaneous reduction in IFT between phase A and the solid surface, from γ_{A_0} to γ_{A_s}. The numerical solution is presented in Fig. 4. The new contact angle measured using the 2D section in Fig. 4b appears to be on the order of 75°. The theoretical one calculated from (90) with the known values of $\gamma_{As} - \gamma_B$ and γ_{AB} gives 77°, which makes a good correspondence with the numerical result.

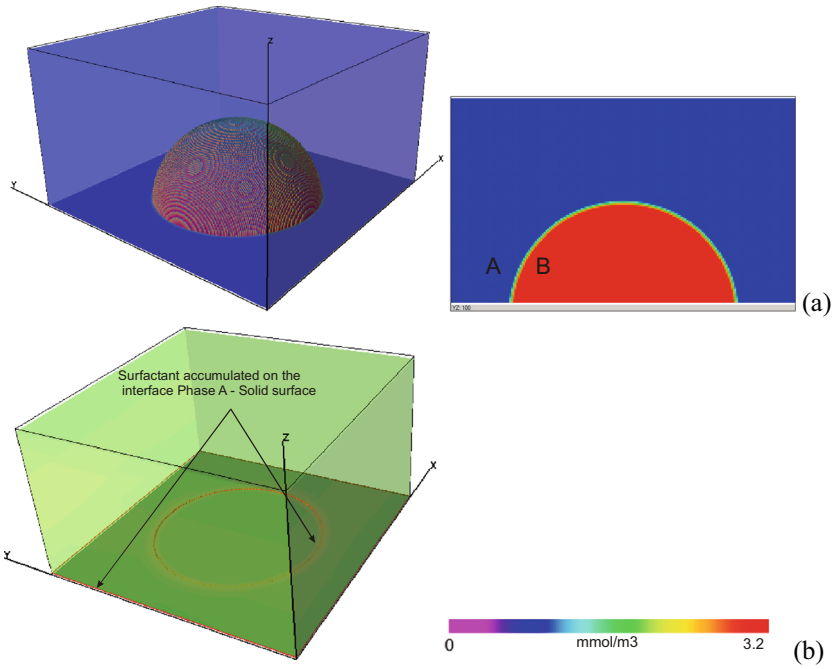

Fig. 4 The sessile drop in the presence of surfactant acting on the liquid-solid interface. **a** Steady-state distribution of component 1 concentration in the presence of a surfactant; **b** steady-state distribution of the surfactant molar density. The *left-hand column* show 3D views of the model, while the *right-hand column* shows the 2D view inside of the section passing through $y = 0.005$ m parallel to the xz-plane. In (**a**), phase A is shown in *semitransparent blue*, phase B in *red*, and the *other colors* indicate the transition zone. In (**b**), the colors correspond to the color palette with the range $n_s \leq 1.5$ mmol/m^3 being semitransparent in the 3D view

To conclude this discussion, we note that the different surfactant mechanisms considered have changed the contact angle in the opposite ways. Indeed, the first mechanism affects the numerator of Eq. 93, while the second one influences the denominator.

6.3 Elongation and breakup of a drop in a shear flow

The behavior of a drop placed in a shear flow has been extensively studied and reported in the literature. Both experimental and theoretical works are abundant. Therefore, such a problem is an excellent numerical modeling demonstration.

The behavior of the drop is determined by the flow parameters and properties of the liquids. Here, we follow the description methodology from the review articles by Rallison [48] and Stone [55].

Suppose that a liquid drop of phase B is suspended inside an ambient liquid phase A. A simple shear (Couette) flow imposed upon phase A, is quantified using the concept of a capillary number (Ca), which is defined by $\mathrm{Ca} = \eta_{sA} G a \gamma_{AB}^{-1}$, where η_{sA} is the ambient liquid shear viscosity, G is a typical shear rate in the neighborhood of the drop, a is the non-deformed drop radius, and γ_{AB} is the IFT. Another important characteristic parameter is the ratio of the drop viscosity and the ambient liquid viscosity expressed by $\bar{\eta} = \eta_{sB} \eta_{sA}^{-1}$. According to the review by Stone [55], one can distinguish several principal regimes of the drop:

- The drop retains a nearly spherical shape. Such a regime is possible when Ca approaches zero. But more interestingly, the spherical shape is still possible at a high value of Cawhen the viscosity ratio $\bar{\eta}$ is sufficiently large, i.e., $\bar{\eta} >> 1$. In such cases, circular fluid flow appears inside of the drop and the latter rotates more like a rigid body.
- In intermediate regimes, when $\bar{\eta} \sim 1$ or smaller and Ca is sufficiently high, the drop can undergo significant shape distortions and assume a steady elongated form.
- With even higher Ca values, the elongation process becomes transient and the drop breaks into fragments. The value of Ca where breakup is observed is called the critical capillary number ($\mathrm{Ca_{cr}}$). The typical dependence of $\mathrm{Ca_{cr}}$ on $\bar{\eta}$ for simple shear flow is given by Rallison [48].

We have performed a numerical simulation of this problem using four different datasets (cases 1 through 4, Table 1). The modeling of cases 1 through 3 was carried out in parallelepiped geometry with sizes of 0.03 m × 0.01 m × 0.01 m approximated by 300 × 100 × 100 cubic cells. For

Table 1 Scope of properties of the simulation cases for the problem of the drop elongation and breakup

	Ca	$\bar{\eta}$	D
Case 1	0.014	100	0.017
Case 2	0.14	10	0.17
Case 3	0.28	5	0.33
Case 4	0.71	2	–

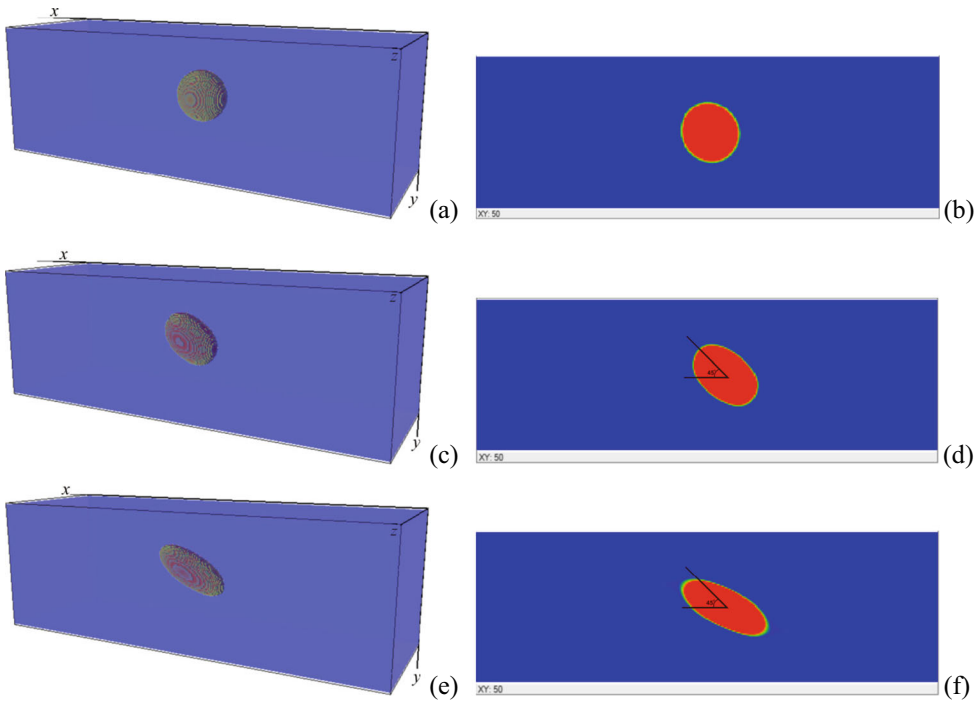

Fig. 5 Elongation of the drop in the shear flow. Steady-state distribution of component 1 concentration; **a**, **b** case 1; **c**, **d** case 2; **e**, **f** case 3. Images (**a**, **c**, **e**) show 3D view of the model, while images (**b**, **d**, **f**) show the phases within 2D section passing $z = 0.005$ m. A reference angle of 45°is indicated on the 2D images. Phase A is shown in *blue* (semitransparent in the 3D views), phase B in *red*, and the *other colors* indicate the transition zone

case 4, a longer model was used with a size of 0.1 m × 0.01 m × 0.01 m approximated with 1000 × 100 × 100 cubic cells. In each case, periodic boundary conditions were applied in the x and y directions. A simple shear flow was imposed by means of the slip boundary conditions specified at the bottom and top sides of the model (at $z = 0$ m and $z = 0.01$ m), where the lateral velocity component v_x was non-zero. The mixture is two-phase two-component; pure component 1 constitutes phase A and pure component 2 forms phase B. In each case, the model was filled with liquid phase A, and a drop of another liquid phase B, having a radius of $a = 0.002$ m, was placed in the geometric center of the corresponding model. The IFT was $\gamma_{AB} = 0.056$ N/m and the shear viscosity of phase B was $\eta_{sB} = 0.1\,\text{Pa} \cdot \text{m}$. Both Ca and $\bar{\eta}$ were varied by changing the shear viscosity of phase A. The scope of Ca and $\bar{\eta}$ used in the simulations is given in Table 1.

The results of the numerical simulations for cases 1 through 4 are presented in Figs. 5 and 6. In cases 1 through 3 (Fig. 5), the steady-state solution exists, while in case 4 (Fig. 6), the solution is transient. In Fig. 5, 2D sections of the model are presented in addition to 3D views. These 2D sections are convenient for quantitative analysis of the simulation results.

As expected, the shape of the drop in case 1 is nearly spherical, while in cases 2 and 3, the drop becomes visibly elongated. As was first demonstrated by Taylor [56], when $\text{Ca} << 1$,the drop shape factor converges to $D = \text{Ca}(19\bar{\eta} + 16)(16\bar{\eta} + 16)^{-1}$, where $D$is defined using the drop length $(2A)$ and breadth $(2B)$ $D = (A - B)(A + B)$. The values of $D$for cases 1 through 3 are given in the third column of Table 1. Figure 5 shows a good agreement between the simulation results and the theory.

Guido and Greco [26] provided the theory and the experimental data on the drop orientation measured as an angle between the major axis of the drop and the flow direction. For small values of Ca, this angle is very close to 45°, while with an increase of Ca, the angle decreases. Our simulation results show the same trend (compare 2D cross sections in Fig. 5b, d, e).

The simulation results of the transient case 4 are presented in Fig. 6. Initially, the drop becomes more and more elongated (b, c); then, the necking structure appears (d); and finally, the drop breaks up and forms satellite drops (e). The entire simulated configuration, including the satellite drops, is remarkably close to the experimental observations presented in [55].

According to the experimental diagram from [49] to [48], the value of Ca_{cr} for $\bar{\eta} = 2$ (as is in Case 4) is ~ 0.5. Our simulations with $\text{Ca} = 0.71$ in case 4 do not contradict those observations.

6.4 Three-phase flow with mobile solid phase

We will now consider the flow of a three-phase mixture containing two liquid phases (A and B) and one mobile solid (elastic) phase (C). In our earlier papers, we have explained the DFH modeling principles for both three-phase mixtures [18] and mixtures containing mobile solid phases [17].

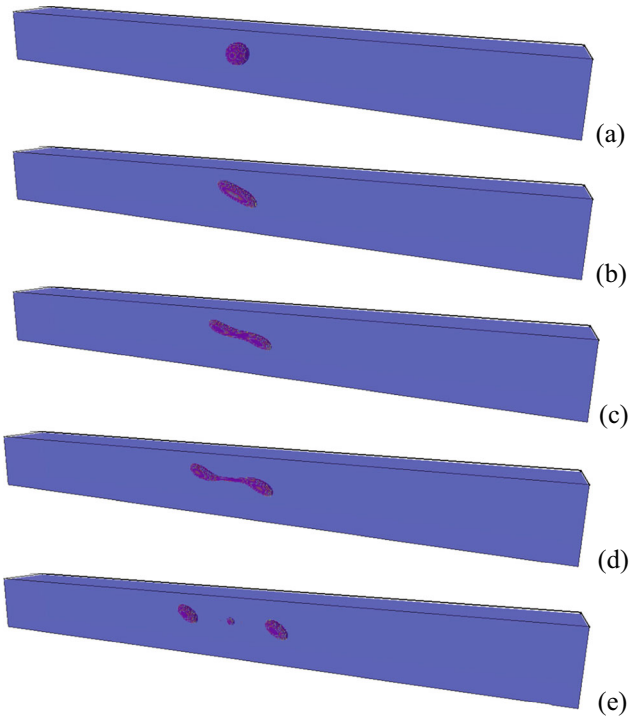

Fig. 6 Case 4—Breakup of the drop in the shear flow. 3D view of the transient distributions of phases at consecutive moments in time; phase A is shown in *semitransparent blue*, phase B in *red*, and the *other colors* indicate the transition zone

In this demonstrational scenario, the flow is arranged inside of a hollow rectangular parallelepiped model with dimensions 0.02 m × 0.02 m × 0.012 m along the $x-$, $y-$, and$z-$axes, respectively. The model is approximated by $200 \times 200 \times 120$ cubic cells. The lower third of the model (i.e., 0 m $\le z \le$ 0.004 m) is filled initially with a liquid phase A, and the rest is filled with a liquid phase B. Furthermore, a solid torus-shaped body (phase C) is placed on the interfacial boundary in such a way that a half of the torus is within one of the liquid phases and the second half is immersed in another liquid phase (Fig. 7a). The height of the torus is 0.002 m, its internal radius is 0.0019 m, and the external radius is 0.0039 m.

The three-phase three-component mixture with phases A, B, and C is such that phase A contains 100 % of the component 1, phase B contains 100 % of component 2, and phase C contains 100 % of the component 3. The relevant parameters of the phases are as follows: $\eta_{\mathrm{s\,A}} = \eta_{\mathrm{s\,B}} = 0.001$ Pa · s, $\eta_{\mathrm{v\,A}} = \eta_{\mathrm{v\,B}} = 0.01$ Pa · s, $\mu_{\mathrm{C}} = 10^6$ Pa, and$\lambda_{\mathrm{C}} = 10^6$ Pa, where $\eta_{\mathrm{s\,A}}$ and $\eta_{\mathrm{v\,A}}$ and $\eta_{\mathrm{s\,B}}$ and $\eta_{\mathrm{v\,B}}$ are shear and volume viscosities of phases A and B, respectively, and μ_{C} and λ_{C} are the Lame coefficients of phase C. The IFTs between each pair of phases are $\gamma_{\mathrm{AB}} = 0.045$ N/m, $\gamma_{\mathrm{CA}} = 0.049$ N/m, and $\gamma_{\mathrm{BC}} = 0.039$ N/m.

The fluid flow within the model was arranged by periodic injection of phases A and B at two sides of the model. To match the injection, the corresponding withdrawal of the liquid was arranged at the opposite sides. In particular, phase A was injected into the rectangle $R_1 = \{x = 0\,\mathrm{m},\ 0\ \mathrm{m} \le y \le 0.016\ \mathrm{m},\ 0\ \mathrm{m} \le z \le 0.004\ \mathrm{m}\}$, while withdrawal of the liquid was made from the rectangle $R_2 = \{x = 0.02\ \mathrm{m},\ 0\,\mathrm{m} \le y \le 0.02\ \mathrm{m},\ 0.004\,\mathrm{m} \le z \le 0.008\,\mathrm{m}\}$. Phase B was injected into the rectangle $R_3 = \{x = 0.02\ \mathrm{m},\ 0.004\ \mathrm{m} \le y \le 0.02\ \mathrm{m},\ 0.004\ \mathrm{m} \le z \le 0.008\ \mathrm{m}\}$, and withdrawal of the liquid was made from the rectangle $R_4 = \{x = 0\,\mathrm{m},\ 0\ \mathrm{m} \le y \le 0.02\ \mathrm{m},\ 0\ \mathrm{m} \le z \le 0.004\ \mathrm{m}\}$. The period of

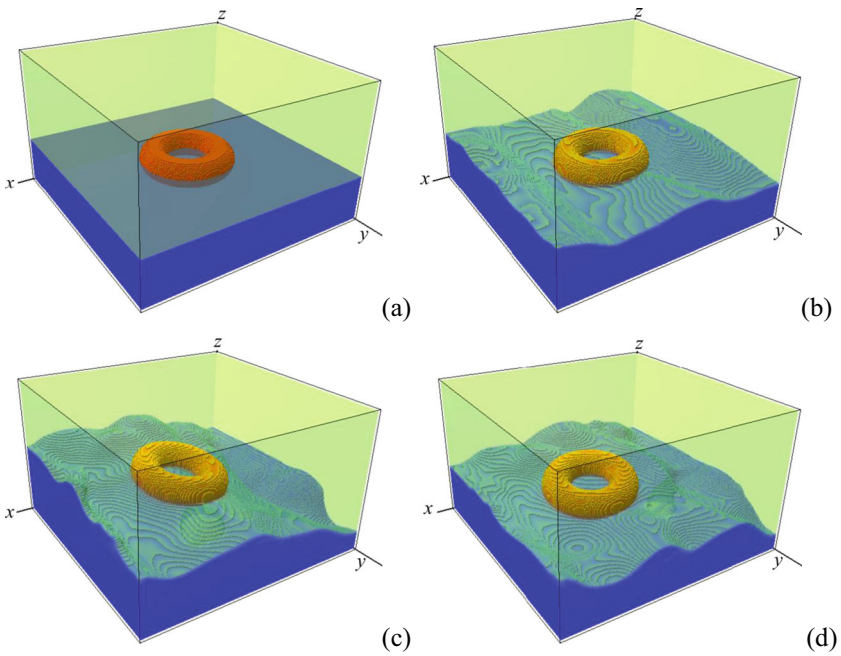

Fig. 7 3D view of the distribution of phases at initial conditions (**a**), and three consecutive time moments 0.03 s (**b**), 0.075 s (**c**), and 0.12 s (**d**); phase A (liquid) is shown in *semitransparent blue*, phase B (liquid) in *semitransparent green*, and phase C (solid) in *red*; the *other colors* indicate the transition zone

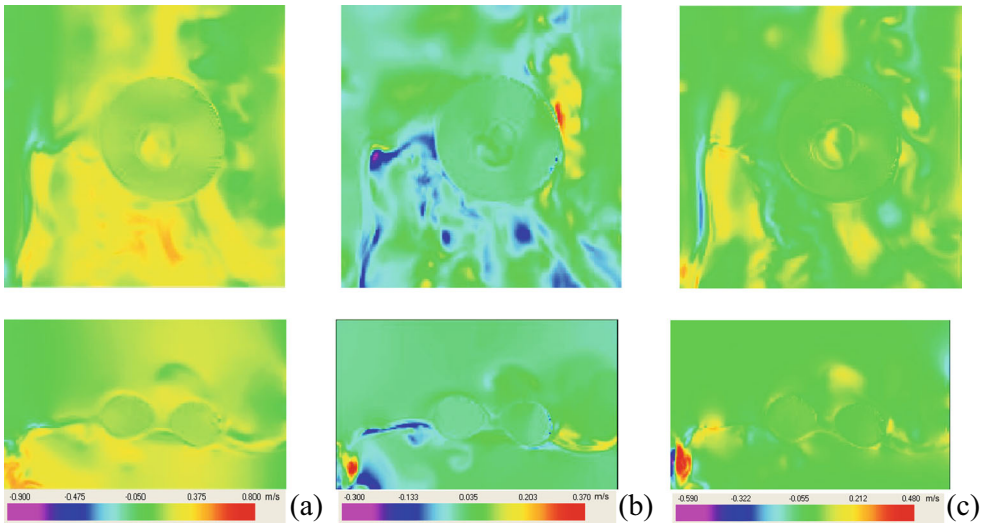

Fig. 8 Distributions of velocity component v_x (**a**), v_y (**b**), and v_z (**c**) at the time moment 0.075 s; the distributions shown within 2D sections of the model passing at $z = 0.0045$ m parallel to the *xy*-plane (*upper row*) and at $y = 0.009$ m parallel to the *xz*-plane (*lower row*). The velocity magnitude is depicted according to the shown color palettes

both injection-withdrawal cycles was the same and equal to 0.015 s. The injection rate in both phases was identical and equal to 1.15 l/min. It was assumed that gravity is not acting on the model.

The results of the numerical simulation of this problem are presented in Figs. 7 and 8. As a result of the cyclic injection-withdrawal procedure, a complex quasi-periodic flow with capillary waves on the two-phase liquid-liquid interface was formed inside of the model. Meanwhile, phase C maintained its initial torus shape and was moving as a solid body. In Fig. 8, we present an instantaneous longitudinal, v_x, and transverse, v_y, v_z, velocity component distributions within several 2D sections of the model. The velocity distributions clearly demonstrate the presence of the toroid solid body within the flow. Moreover, the velocity fields in the liquid and inside of the solid body are continuous and in concert with each other. Inside of the solid body, the necessary equalities $\partial_a v_b + \partial_b v_a = 0$ are fulfilled.

7 Examples of pore-scale multiphase flow

In this section, we demonstrate typical applications, where our modeling method, DFH, can be efficiently employed. Both examples presented here are related to the so-called digital rock (DR) modeling technique, which is an emerging method for the non-destructive description of the pore-scale processes within porous rocks. The concept of DR is discussed in many papers; for example [3, 30, 35, 36, 49, 51]. In a nutshell, the DR approach is contained in the following steps:

- X-ray scanning of a rock sample (core) at a high micro- or nanometer resolution.
- Construction of a 3D digital model of the scanned sample; the model contains information about resolved pores and mineralogical composition.
- Pore-scale numerical simulation of the processes relevant to the core.

While the contents of the first two steps are determined mostly by the type of the available equipment, the essence of the last step is shaped by the modeling methodology, which is applied for the pore-scale processes simulation. The methodology that we use is that of DFH.

7.1 Two-phase immiscible water-oil flow

We begin with the description of an immiscible two-phase flow. The flow occurs in pores of a sandstone core sample taken from Cenomanian formation of one of the Western Siberia oilfields. The 3D DR model constructed for this sample has porosity equal to 22.2 % and absolute permeability equal to 210 mD. The model is a cube; the size of an edge is 2.1 mm. The model resolution is 2.67 μm, which is the same as the voxel resolution of the X-ray scanning done for the sample. Thus, the computational grid of the DR model contains 800^3, or just over half a billion, cubic cells (Figure 9a).

The fluids used in the modeling were water (phase A) and oil (phase B) with the following relevant properties: $\eta_{s\,A} = 0.001$ Pa·s, $\eta_{s\,B} = 0.00092$ Pa·s, $\gamma_{AB} = 0.029$ N/m, where $\eta_{s\,A}$ and $\eta_{s\,B}$ are shear viscosities of phases A and B and γ_{AB} is the water-oil IFT.

The wettability boundary conditions were specified over entire rock surface by a stochastic Gaussian distribution of the Helmholtz surface energy density with correlation radius on the order of two mean pore sizes. The maximum surface energy for oil was 0.3 N/m and 0.1 N/m for water.

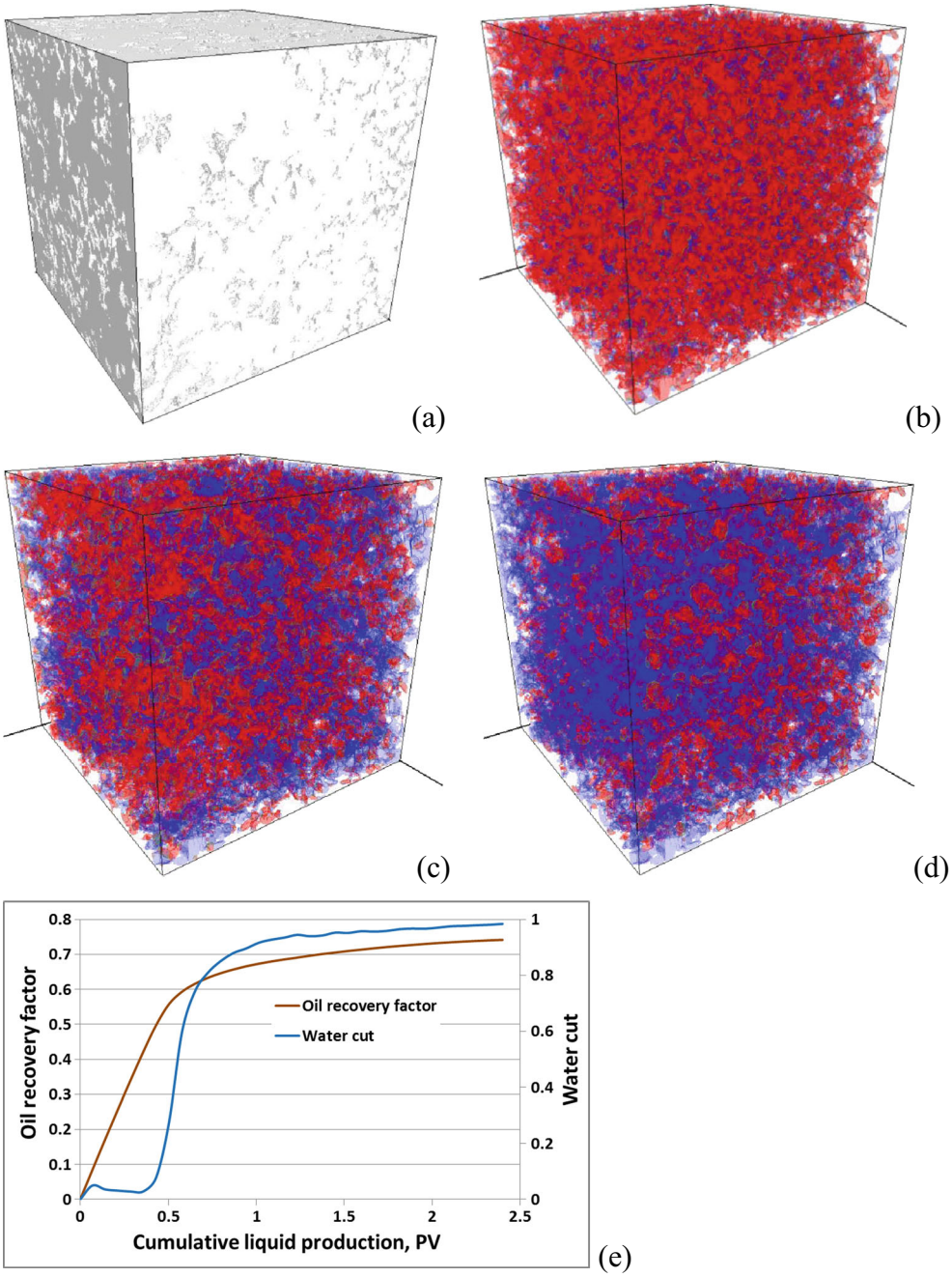

Fig. 9 The DR model of the Cenomanian Berea sandstone sample. 3D view of the **a** rock. Distribution of oil and water at **b** initial equilibrium conditions, **c** an intermediate stage of the water flood, and **d** after the water flood; in (**b**–**d**), water is shown in *semitransparent blue* and oil in *semitransparent red*, while rock is removed from view. **e** Oil recovery factor and water cut as the functions of cumulative liquid production in pore volumes (*PV*)

Therefore, the model was mixed-wet with a bigger portion of rock wet by water.

Initially, oil and water were randomly distributed within the pores with average water saturation equal to 22 %. Then the numerical simulation on the closed model (all six models' sides are impermeable) was performed to let the phases come to equilibrium with the local wetting properties. The resulting distribution of phases (Fig. 9b) was used as initial conditions for the two-phase flow simulation.

The flow was arranged to mimic a typical oil recovery scenario using water flood. Four sides of the model were left impermeable, while the rest two opposite sides were opened. At one of the open sides, a constant ref-

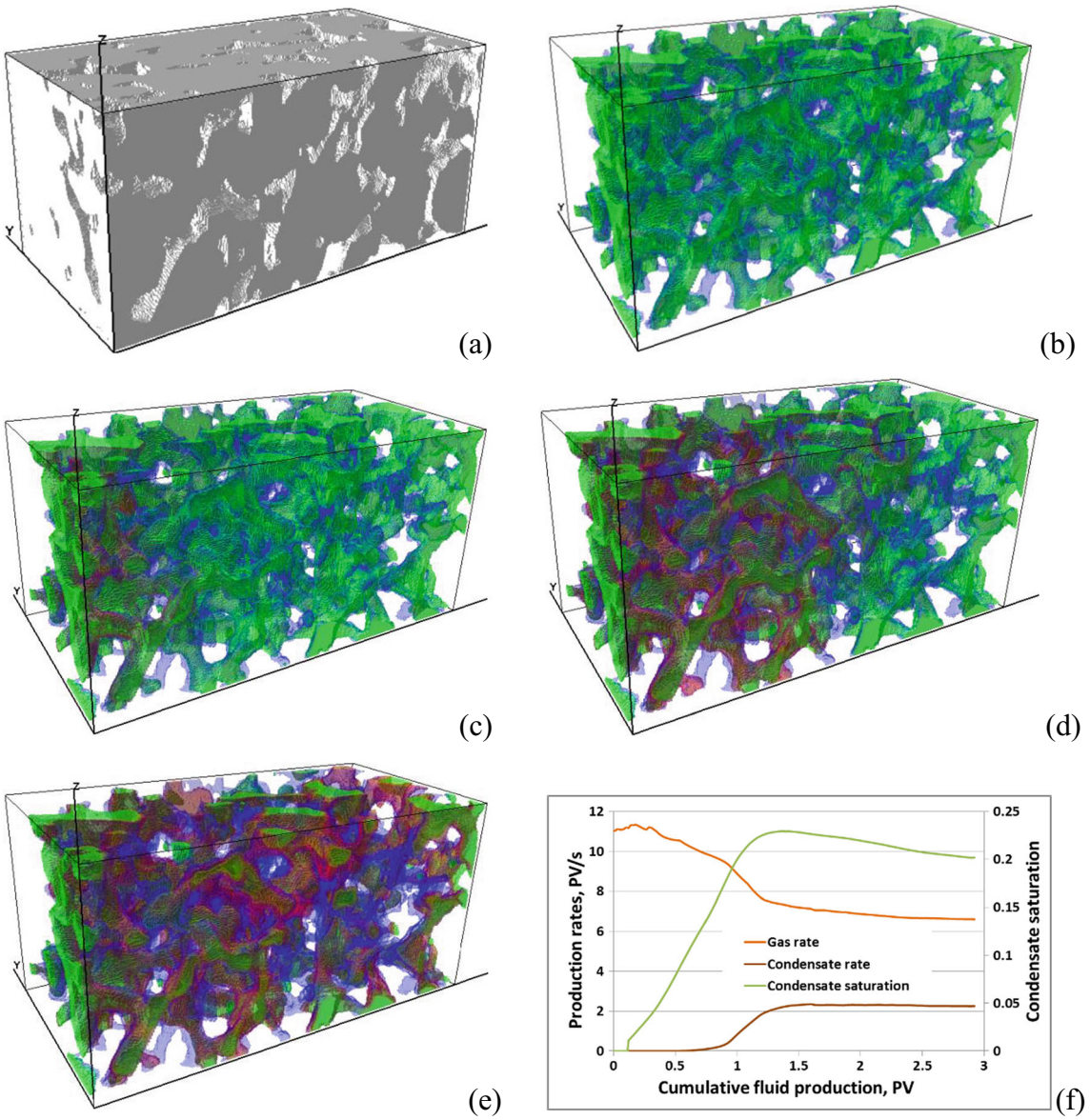

Fig. 10 The DR model of the gas-condensate field Berea sandstone sample. 3D view of the **a** rock, distribution of gas, and water at **b** initial reservoir conditions; distribution of gas, condensate, and water at **c**, **d** an intermediate stage of the production and **e** after stabilization of the production rates; in (**b**–**e**), water is shown in *semitransparent blue*, gas in *semitransparent green*, and condensate in *semitransparent red*; rock is removed from view. **f** Gas and condensate production rates in pore volumes (*PV*) per second and overall condensate saturation as the functions of cumulative fluid production in PV

erence pressure was sustained, while on the other side water was injected by connecting an infinite-volume water reservoir held at a constant pressure 1000 Pa above the reference value. Given the size of the model, this corresponds to the pressure gradient about 5 bar/m. The simulation was carried out till the moment when water cut has exceeded 98 %.

Figure 9c–e show the flow simulation results. The flow occurs from right to left as seen in the figures. Figure 9d shows the distribution of residual oil and water after about 2.4 pore volumes (PV) of water pumped through, while Fig. 9c shows an intermediate state after about 0.4 PV. The chart in Fig. 9e demonstrates the recovery factor (i.e., ratio of cumulative volumetric oil produced to the initial volumetric oil in place) and the water cut (i.e., ratio of volumetric water production rate to volumetric liquid production rate) as the functions of the cumulative liquid production. The recovery factor reached at 98 % water cut appeared to be about 74 %, which corresponds to about 20 % of the residual oil saturation.

7.2 Non-equilibrium three-phase flow

In this subsection, we consider three-phase water-gas-condensate flow with phase transitions. The flow occurs in pores of a Berea sandstone core sample. The 3D DR model constructed for this sample has porosity equal to 22.5 % and absolute permeability equal to 830 mD. The model is a parallelepiped with sizes 0.69 mm × 0.35 mm × 0.35 mm along the $x-$, $y-$, and $z-$axes, respectively. The model is approximated by 300 × 150 × 150 cubic cells and has resolution of 2.67 μm, which is the same as the voxel resolution of the X-ray scanning done for the sample (Fig. 10a).

The fluids used in the modeling were water (phase A), gas (phase B), and condensate (phase C) with the following relevant properties: $\eta_{s\,A} = 0.001$ Pa·s, $\eta_{s\,B} = 2\times10^{-5}$ Pa·s, $\eta_{s\,C} = 5\times10^{-4}$ Pa·s, $\gamma_{AB} = 0.019$ N/m, $\gamma_{AC} = 0.017$ N/m, $\gamma_{BC} = 0.005$ N/m, where $\eta_{s\,A}$, $\eta_{s\,B}$, and $\eta_{s\,C}$ are shear viscosities of phases A, B, and C and γ_{AB}, γ_{AC}, and γ_{BC} are the IFT values between pairs of phases AB, AC, and BC. The mixture is described by three pseudocomponents—one per each phase.

The simulated scenario corresponds to the typical situation happening during the later stages of a gas-condensate reservoir production when pressure drops below the dew point. Initially, a typical gas-condensate reservoir contains only two-phase mixture—one phase is water and another phase is gas containing both light and heavy hydrocarbons. During the development, pressure drops gradually below the dew point. At that moment, dropout of condensate begins. Condensate accumulates gradually within some of the pores and hinders the gas flow. Such situation is known as condensate banking.

To model the described scenario, we pumped a heavy gas-condensate mixture (i.e., with high proportion of heavy components) having the composition corresponding to the initial reservoir conditions through the DR model in the lateral direction (along the x-axis). The pumping occurs due to the assumed lateral pressure drawdown equal to 80 Pa.

The wettability boundary conditions were specified over entire rock surface by a stochastic Gaussian distribution of the Helmholtz surface energy density with correlation radius on the order of two mean pore sizes. The minimum and maximum surface energies for condensate were 0.15 and 0.2 N/m, and for gas they were 0.25 and 0.3 N/m, respectively. Therefore, the model was strongly wet by water with forming a water film (zero contact angle). At the same time, in the presence of both gas and condensate, the latter needs less energy than the former to come into contact with rock.

Initially, gas and water were randomly distributed within the pores with average water saturation equal to 10 %. Then the numerical simulation on the closed model (all six models' sides impermeable) was performed to let the phases come to equilibrium with the local wetting properties. The resulting distribution of phases (Fig. 10b) was used as initial conditions for the flow simulation.

In the flow simulation, the four lateral sides of the model were left impermeable, while the two transverse sides were opened. The flow was in the positive x-direction (from left to right in Fig. 10c–e). The simulation was carried out until stabilization of the gas and condensate production rates (Fig. 10f).

Figure 10c–e shows gradual grows of condensate dropout (semitransparent red). Eventually, the flow reaches quasi-steady regime, in which time average production rates of both gas and condensate become constant. At the same time, overall condensate saturation stabilizes at about 20 %. This 20 % of condensate constitutes the accumulated condensate bank, which hinders the fluid flow and negatively impacts the production.

8 Discussion and conclusions

The presented results demonstrate that the DFT approach in multiphase hydrodynamics is able to handle effectively the variety of two-phase and three-phase problems including phase transitions and surfactants. Since the presented method is rigorously derived from the first principles, it is consistent with classical chemical thermodynamics. It is applicable and effective in both simple geometries and complex pore-scale models.

The important fact is that all the simulations were carried out by the same numerical code. In every case, the same system of equations was solved numerically by the same procedure. It has been necessary only to set up the number of chemical components, parameters of density functional, boundary conditions, and rheological parameters. This flexibility is very convenient in practice. Also, it provides the consistency between three-phase, two-phase, and one-phase simulations.

In this paper, we have presented only the basic and typical examples of DFT applications. The scope of physical phenomena covered by DFT is continuously growing with ever more chemically and physically complex cases coming under consideration. In particular, the processes with thermal effects and chemical reactions are presently in intensive study involving validation and benchmarking. Also, the cross-disciplinary modeling is under development, which combines multiphase pore-scale hydrodynamics with nuclear magnetic resonance, electromagnetic and electrokinetic phenomena, microgeomechanics, and X-ray and neutron scattering.

References

1. Anderson, D.M., McFadden, G.B., Wheeler, A.A.: Diffuse-interface methods in fluid mechanics. Annu. Rev. Fluid Mech. **30**, 139–165 (1998)
2. Bazarov, I.: Thermodynamics. Pergamon Press, Oxford (1964)
3. Berg, S., Armstrong, R., Ott, H., Georgiadis, A., Klapp, S.A., Schwing, A., Neiteler, R., Brussee, N., Makurat, A., Leu, L., Enzmann, F., Schwarz, J.-O., Wolf, M., Khan, F., Kersten, M., Irvine, S., Stampanoni, M.: Multiphase flow in porous rock imaged under dynamic flow conditions with fast x-ray computed microtomography SCA2013-011, Napa Valley, California, USA
4. Davydov, Yu.M.: Calculation by the coarse particle method of the flow past a body of arbitrary shape. USSR Comp. Math. Math. Phys **11**(4), 304–312 (1972)
5. de Groot, S.R., Mazur, P.: Non-Equilibrium Thermodynamics. Dover, New York (2011)
6. de Wit, R.: Theory of disclinations: III. Continuous and discrete disclinations in isotropic elasticity. J. Res. Natl. Bur. Stand. **77A**(3), 359–368 (1973)
7. Demyanov, A.Yu., Dinariev, O.Y.u.: Modeling of multicomponent multiphase mixture flows on the basis of the density functional method. Fluid Dyn. **39**(6), 933–944 (2004)
8. Dem'yanov, A.Yu., Dinariev, O.Y.u.: Application of the density-functional method for numerical simulation of flows of multi-species multiphase mixtures. J. Appl. Mech. Tech. Phys **45**(5), 670–678 (2004)
9. Demianov, A.Yu., Dinariev, O.Yu., Evseev, N.V.: Introduction to the density functional theory in hydrodynamics. Fizmatlit, Moscow (2014)
10. Demianov, A., Dinariev, O., Evseev, N.: Density functional modeling in multiphase compositional hydrodynamics. Can. J. Chem. Eng. **89**, 206–226 (2011)
11. Dinariev, O.Y.: A hydrodynamic description of a multicomponent multiphase mixture in narrow pores and thin layers. J. Appl. Math. Mech **59**(5), 745–752 (1995)
12. Dinariev, O.Y.: Thermal effects in the description of a multicomponent mixture using the density functional method. J. Appl. Math. Mech **62**(3), 397–405 (1998)
13. Dinariev, O.Y.u.: Nonnegative entropy production in the hydrodynamics of multiparticle quantum system. Russ. Phys. J. **41**(5), 60–66 (1998)
14. Dinariev, O.Y.u.: Nonnegative hydrodynamic entropy production in classical statistical mechanics. Russ. Phys. J. **43**(12), 1044–1048 (2000)
15. Dinariev, O.Y.u.: Substantiation of the method of density functional in classical and quantum statistical mechanics. Russ. Phys. J. **43**(9), 713–717 (2000)
16. Dinariev, O.Yu., Evseev, N.V.: Description of the flows of two-phase mixtures with phase transitions in capillaries by the density-functional method. J. Engineer. Phys. Thermophys. **78**(3), 474–481 (2005)
17. Dinariev, O.Y.u., Evseev, N.V.: Description of viscous-fluid flows with a moving solid phase in the density-functional theory. J. Engineer. Phys. Thermophys. **80**(5), 70–77 (2007)
18. Dinariev, O.Yu., Evseev, N.V.: Application of density-functional theory to calculation of flows of three-phase mixtures with phase transitions. J. Engineer. Phys. Thermophys. **80**(6), 1247–1255 (2007)
19. Dinariev, O.Yu., Evseev, N.V.: Modeling of surface phenomena in the presence of surface-active agents on the basis of the density-functional theory. Fluid Dyn. **45**(1), 85–95 (2010)
20. Dreizler, R.M., Gross, E.K.U.: Density Functional Theory: An Approach to Quantum Many-Body Problem. Springer, Berlin (1990)
21. Eringen, A.C., Suhubi, E.S.: Elastodynamics, vol. 1. Finite Motions. Academic Press, New York (1974)
22. Eschrig, H.: The fundamentals of density functional theory. Teubner, Stuttgart (1996)
23. Fermi, E.: Un Metodo Statistice per la Determinazionedi Alcune Proprieta dell'Atomo. Rend. Accad. Lincei **6**, 602–607 (1927). (in Italian)
24. Gelfand, I.M., Fomin, S.V.: Calculus of Variations. Dover, New York (2003)
25. Gray, R.M.: Entropy and Information Theory. Springer, New York (1990)
26. Guido, S., Greco, F.: Dynamics of a liquid drop in a flowing immiscible liquid. In: Rheology Reviews, pp. 99–142 (2004)
27. Hohenberg, P., Kohn, W.: Inhomogeneous electron gas. Phys. Rev. **3B**(136), 864–871 (1964)
28. Kadić, A., Edelen, D.G.B.: A Gauge Theory of Dislocations and Disclinations. Springer, Berlin (1983)
29. Kleinert, H.: Gauge Fields in Condensed Matter, vol. 2. Stresses and Defects. World Scientific, Singapore (1989)
30. Knackstedt, M., Senden, T., Carnerup, A., Fogden, A.: Improved characterization of EOR processes in 3D. Characterizing mineralogy, wettability and residual fluid phases at the pore scale. In: Proceedings of the SPE Enhanced Oil Recovery Conference. 19-21 July, Kuala Lumpur, Malaysia, SPE 145093 (2011)
31. Koch, W., Holthausen, M.C.: A Chemist's Guide to Density Functional Theory. Wiley, Weinheim (2001)
32. Kohn, W., Sham, L.J.: Self consistent equations including exchange and correlation effects. Phys. Rev **140**, A1133—A1138 (1965)
33. Konopleva, N.P., Popov, V.N.: Gauge Fields. Harwood Academic Publ., New York (1981)
34. Korobeinikov, S.N.: Nonlinear deformation of solids. Siberian Division of RAS, Novosibirsk (2000). (in Russian)
35. Koroteev, D., Dinariev, O., Evseev, N., Klemin, D., Nadeev, A., Safonov, S., Gurpinar, O., Berg, S., van Kruijsdijk, C., Armstrong, R.T., Myers, M.T., Hathon, L., de Jong, H.: Direct hydrodynamic simulation of multiphase flow in porous rock. In: Proceedings of the International Symposium of the Society of Core Analysts, SCA2013-014, Napa Valley, California, USA (2013)
36. Koroteev, D., Dinariev, O., Evseev, N., Klemin, D., Safonov, S., Gurpinar, O., Berg, S., van Kruijsdijk, C., Myers, M., Hathon, L., de Jong, H.: Application of digital rock technology for chemical EOR screening. In: Proceedings of the SPE Enhanced Oil Recovery Conference. 2-4 July, Kuala Lumpur, Malaysia, SPE-165258 (2013)
37. Kossevich, A.M.: The Crystal Lattice. Wiley, Berlin (1999)
38. Kröner, E.: Allgemeine Kontinuumstheorie der Versetzungen und Eigenspannungen. Arch. Ration. Mech. Anal. **4**(4), 18–334 (1960). (in German)
39. Kunin, I.A.: Theory of dislocations. In: Schouten, J.A. (ed.) Tensor Analysis for Physicists. (in Russian), pp. 373–443. Moscow, Nauka (1965)
40. Lamb, H. Statics, Including Hydrostatics and the Elements of the Theory of Elasticity, 3rd ed. Cambridge University Press, Cambridge (1928)
41. Lurie, A.I.: Nonlinear Theory of Elasticity. North-Holland, Cambridge, England (1990)
42. Martin, N.F.G., England, J.W.: Mathematical Theory of Entropy. Cambridge University Press, Cambridge (2010)

43. Mura, T.: Micromechanics of Defects in Solids. Martinus Nijhoff Publ., Dordrecht (1987)
44. Murnagan, F.D.: Finite Deformations of Elastic Solid. Wiley, New York (1951)
45. Parr, R.G., Yang, W.: Density-Functional Theory of Atoms and Molecules. Oxford University Press, Oxford (1989)
46. Patankar, S.: Numerical Heat Transfer and Fluid Flow. Hemisphere Publishing Corporation, New York (1980)
47. Prigogine, I., Defay, R.: Chemical Thermodynamics. Longman, New York (1954)
48. Rallison, J.M.: The deformation of small viscous drops and bubbles in shear flows. Ann. Rev. Fluid Mech **16**, 45–66 (1984)
49. Rassenfoss, S.: Digital rocks out to become a core technology. J. Pet. Technol., 36–41 (2011)
50. Rosen, M.I.: Surfactants and Interfacial Phenomena. Wiley, Hoboken (2004)
51. Saenger, E.H., Madonna, C.: Digital rock physics: numerical vs. laboratory measurements. In: Proceedings of the SEG Annual Meeting, San Antonio TX, USA, 18-23 September (2011)
52. Sedov, L.I.: Mechanics of continuous media, vol. 1. World Scientific, New York (1996)
53. Steinbach, I.: Phase-field model for microstructure evolution at the mesoscopic scale. Annu. Re. Mater. Res **43**(1), 89–107 (2013)
54. Sternberg, S.: Lectures on Differential Geometry. Chelsea Pub Co., London (1982)
55. Stone, H.A.: Dynamics of drop deformation and breakup in viscous fluids. Annu. Rev. Fluid Mech **26**, 65–102 (1994)
56. Taylor, G.I.: The viscosity of a fluid containing small drops of another fluid. Proc. R. Soc. London Ser. A **38**, 41–48 (1932)
57. Thomas, L.H.: The calculation of atomic fields. Proc. Camb. Philos. Soc. V. **23**, 542–548 (1927)
58. Truesdell, C., Noll, W.: The Non-Linear Field Theories of Mechanics. Springer, Berlin (2004)
59. Zubarev, D.: Nonequilibrium Statistical Thermodynamics. Springer, New York (1974)